



## The Perdigão: Peering into Microscale Details of Mountain Winds

**Fernando, H.J.S.; Mann, Jakob; Palma, J.M.L.M.; Lundquist, J.K.; Barthelmie, Rebecca Jane; BeloPereira, M.; Brown, W.O.J.; Chow, F.K.; Gerz, T.; Hocut, C.M.**

*Total number of authors:*  
48

*Published in:*  
Bulletin of the American Meteorological Society

*Link to article, DOI:*  
[10.1175/BAMS-D-17-0227.1](https://doi.org/10.1175/BAMS-D-17-0227.1)

*Publication date:*  
2019

*Document Version*  
Publisher's PDF, also known as Version of record

[Link back to DTU Orbit](#)

### *Citation (APA):*

Fernando, H. J. S., Mann, J., Palma, J. M. L. M., Lundquist, J. K., Barthelmie, R. J., BeloPereira, M., Brown, W. O. J., Chow, F. K., Gerz, T., Hocut, C. M., Klein, P. M., Leo, L. S., Matos, J. C., Oncley, S. P., Pryor, S. C., Bariteau, L., Bell, T. M., Bodini, N., Carney, M. B., ... Wang, Y. (2019). The Perdigão: Peering into Microscale Details of Mountain Winds. *Bulletin of the American Meteorological Society*, 100(5), 799-820. <https://doi.org/10.1175/BAMS-D-17-0227.1>

---

### General rights

Copyright and moral rights for the publications made accessible in the public portal are retained by the authors and/or other copyright owners and it is a condition of accessing publications that users recognise and abide by the legal requirements associated with these rights.

- Users may download and print one copy of any publication from the public portal for the purpose of private study or research.
- You may not further distribute the material or use it for any profit-making activity or commercial gain
- You may freely distribute the URL identifying the publication in the public portal

If you believe that this document breaches copyright please contact us providing details, and we will remove access to the work immediately and investigate your claim.

# THE PERDIGÃO

## Peering into Microscale Details of Mountain Winds

H. J. S. FERNANDO, J. MANN, J. M. L. M. PALMA, J. K. LUNDQUIST, R. J. BARTHELMIE, M. BELO-PEREIRA, W. O. J. BROWN, F. K. CHOW, T. GERZ, C. M. HOCUT, P. M. KLEIN, L. S. LEO, J. C. MATOS, S. P. ONCLEY, S. C. PRYOR, L. BARITEAU, T. M. BELL, N. BODINI, M. B. CARNEY, M. S. COURTNEY, E. D. CREEGAN, R. DIMITROVA, S. GOMES, M. HAGEN, J. O. HYDE, S. KIGLE, R. KRISHNAMURTHY, J. C. LOPES, L. MAZZARO, J. M. T. NEHER, R. MENKE, P. MURPHY, L. OSWALD, S. OTAROLA-BUSTOS, A. K. PATTANTYUS, C. VEIGA RODRIGUES, A. SCHADY, N. SIRIN, S. SPULER, E. SVENSSON, J. TOMASZEWSKI, D. D. TURNER, L. VAN VEEN, N. VASILJEVIĆ, D. VASSALLO, S. VOSS, N. WILDMANN, AND Y. WANG

A U.S.–European collaborative field campaign with unprecedentedly dense instrumentation collected data for process, modeling, and wind-resource-mapping studies at microscale.

**D**uring 1 May–15 June 2017, some 70+ scientists, engineers, and support personnel converged on Vale do Cobrão, located in central Portugal within the municipality of Vila Velha de Ródão, for a unique field campaign designed to study microscale details of mountain winds (Fig. 1). Dubbed *Perdigão* (*partridge* in Portuguese) after a nearby village, the campaign culminated a decade-long preparation of European Union (EU) scientists to create a New Digital EU Wind Atlas (NEWA) at microscale resolution (see sidebar). The topography of Vale do Cobrão resembles a textbook case of a two-dimensional (2D) valley within parallel ridges, with annual wind climatology perpendicular to the ridges. Adding value to the site is a lone wind turbine (WT) on the southern ridge. In 2013, a group of investigators from the United States was invited to join with U.S. agency support, forging a productive cross-Atlantic research partnership with complementary goals: understanding and modeling of microscale processes in complex terrain, including wind turbine wakes (U.S. group) and developing skilled microscale models with enhanced wind energy physics that would help NEWA (EU group; Mann et al. 2017). The principal

investigators as well as science drivers are listed in the supplemental material (<https://doi.org/10.1175/BAMS-D-17-0227.2>).

More than 70% of the Earth's land surface is in complex terrain (Strobach 1991), and thus mountain meteorology has attracted the attention of a wide range of constituencies, including climatologists (Gobiet et al. 2014), fluid dynamists (Fernando 2010), and wind engineers (Alfredsson and Segalini 2017). Most past research has been on mesoscales (~1–100 km), spurred by air pollution, aviation, warfare, and energy applications. Large field projects with mesoscale emphasis abound, some examples being Vertical Transport and Mixing (VTMX; Doran et al. 2002), the Terrain-Induced Rotor Experiment (T-REX; Grubišić et al. 2008), MATERHORN (Fernando et al. 2015), and the second Wind Forecast Improvement Project (WFIP-2; Wilczak et al. 2019). More recently, however, microscale flows in complex terrain have received increasing interest owing to growing applications in wind engineering (Clifton et al. 2014), firefighting (Li et al. 2016), and winter sports (Kiktev et al. 2017). Complex terrain is being increasingly pursued for

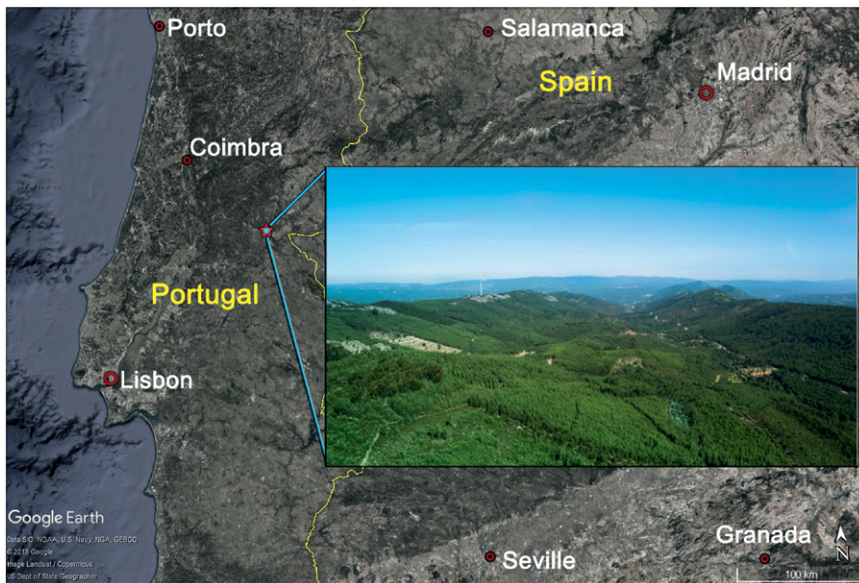


**FIG. 1.** The geographic location of double-ridged Vale do Coirão (red star) in central Portugal. A picture of the valley, looking northwestward (down valley), is in the inset. A single wind turbine is on the southern ridge.

wind farms, especially in Europe, because complex terrain areas are readily found away from human settlements and available flat terrain suitable for wind energy production is at a premium (Alfredsson and Segalini 2017). Complex terrain offers the advantages of wind amplification at ridges, flow jetting through canyons, and remoteness from urban communities with strict noise regulations. Conversely, turbulence levels, gustiness, and wind variability are much higher in complex terrain, stoking challenges to WT operations.

The WT rotors sweep the atmospheric boundary layer (ABL), which is characterized by shear, veer, stratification, gusts, and turbulence. Since

ed in the 1980s (Taylor and Teunissen 1983) and a few small-scale field experiments (Palma et al. 2008; Berg et al. 2011; Lange et al. 2017).

The Perdigão field campaign was designed to gather a comprehensive dataset of unprecedented resolution to address knowledge gaps in wind-energy physics, develop new parameterizations, and help validate models while contributing to NEWA objectives. The campaign location (Fig. 1) offered many advantages, including a (nominally) simple flow configuration. An assemblage of cutting-edge sensors catered the science goals of participants that ranged from multiscale physics studies, to wind mapping at ~25–50-m resolution, to turbine wake investigations,

electricity production is approximately proportional to the cube of wind speed, small errors in wind speed lead to unacceptable errors in energy production estimates. This calls for advances in wind forecasting tools, microscale models in particular, for which field data are imperative for understanding of wind-energy physics and model validation (Ayotte 2008). High-resolution meteorological data are scarce, however, and research and development work over the past three decades have heavily relied on the single-hill Askervein experiment conduct-

**AFFILIATIONS:** FERNANDO, LEO, DIMITROVA, HYDE, KRISHNAMURTHY, OTAROLA-BUSTOS, SIRIN, AND VASSALLO—University of Notre Dame, Notre Dame, Indiana; MANN, COURTNEY, MENKE, SVENSSON, AND VASILJEVIC—Denmark Technical University, Lyngby, Denmark; PALMA, LOPES, AND VEIGA RODRIGUES—University of Porto, Porto, Portugal; LUNDQUIST, BODINI, MAZZARO, MURPHY, AND TOMASZEWSKI—University of Colorado Boulder, Boulder, Colorado; BARTHELMIE AND PRYOR—Cornell University, Ithaca, New York; BELO-PEREIRA AND GOMES—Portuguese Institute of Sea and Atmosphere, Algés, Portugal; BROWN, ONCLEY, AND SPULER—National Center for Atmospheric Research, Boulder, Colorado; CHOW, NEHER, AND VAN VEEN—University of California, Berkeley, Berkeley, California; GERZ, HAGEN, KIGLE, OSWALD, SCHADY, AND WILDMANN—German Aerospace Center, Cologne, Germany; HOCUT, CREEGAN, PATTANTYUS, AND WANG—Army Research Laboratory, Adelphi, Maryland; KLEIN, BELL, AND CARNEY—University of Oklahoma,

Norman, Oklahoma; MATOS—Institute of Science and Innovation in Mechanical and Industrial Engineering, Porto, Portugal; BARITEAU AND TURNER—National Oceanic and Atmospheric Administration/Earth System Research Laboratory, Boulder, Colorado; Voss—University of Oldenburg, Oldenburg, Germany

**CORRESPONDING AUTHOR:** Harindra J. S. Fernando, fernando.10@nd.edu

The abstract for this article can be found in this issue, following the table of contents.

DOI:10.1175/BAMS-D-17-0227.1

A supplement to this article is available online (10.1175/BAMS-D-17-0227.2)

In final form 13 October 2018

©2019 American Meteorological Society

For information regarding reuse of this content and general copyright information, consult the [AMS Copyright Policy](#).

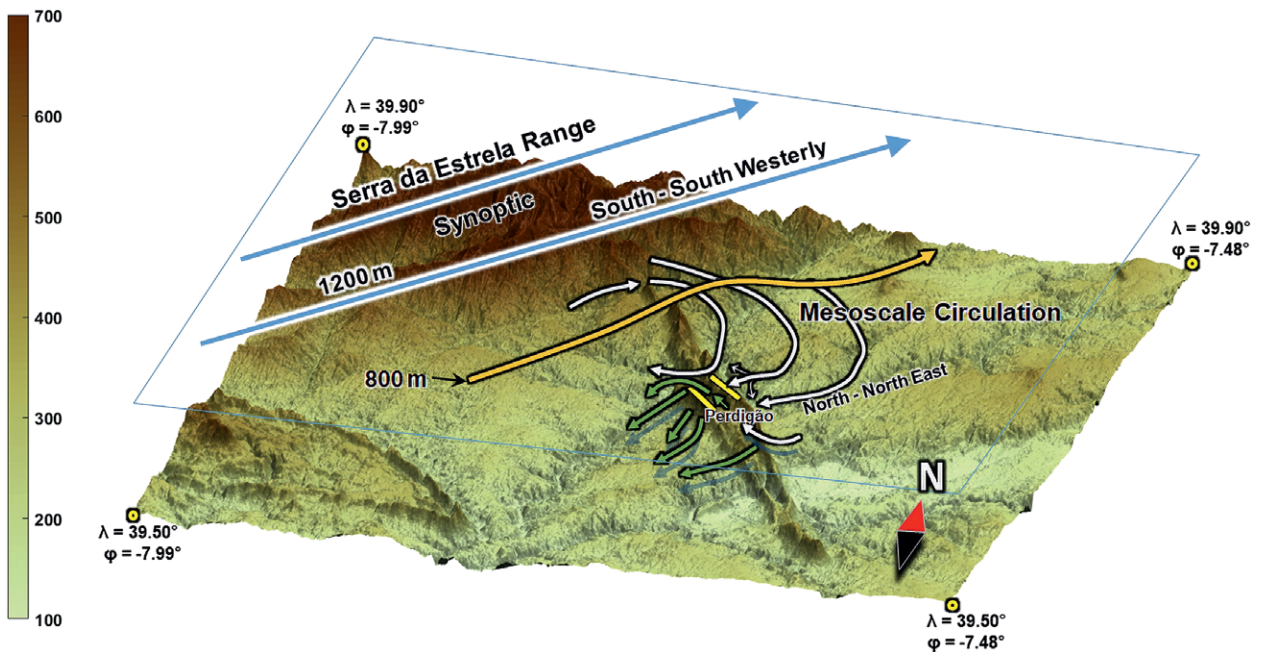


**FIG. 2.** The response of complex-terrain atmospheric boundary layer to south-southwesterly synoptic forcing based on meso- and microscale simulations and Perdigão measurements (see supplemental material). The synoptic flow is influenced by Serra da Estrela (e.g., Lousã-Estrela and Alvelos-Gardunha) mountains to the northwest (~40 km) and by S. Mamede to the southeast. The height of the topography (see color bar), latitude  $\lambda$ , and longitude  $\phi$  are shown. Blue lines show synoptic flow and mustard yellow lines represent synoptic flow disturbed by large-scale topography. Perdigão double ridges are shown by bumblebee-yellow lines. White lines indicate mesoscale flow formed by strong interaction of synoptic flow with large-scale topography, and green shows microscale flows within and surrounding Perdigão ridges swayed by local topography. Other predominant approach flow directions also produce kindred complex 3D flows.

to noise propagation studies. The data are archived in multiple locations and are expected to set the gold standard for microscale model validation studies.

**PROCESSES AND INTERACTIONS.** The design of Perdigão was guided by previous laboratory, theoretical, and numerical studies of (idealized) flow over topographies (Queney 1948; Long 1955; Brighton 1978; Baines 1998; Belcher and Hunt 1998; Boyer and Davies 2000; Castro et al. 2003) as well as field studies (Taylor et al. 1987; Walmsley and Taylor 1996). It was recognized that natural flows tend to be capricious and represent a (nonlinear) mix of processes mingled in a way as to obscure individual phenomena. While Askervein is hailed as close to an idealized axisymmetric topography, studies have found that nearby mountains could influence Askervein flows (Kim and Patel 2000). Similarly, we found that the initially perceived two-dimensional flow in Perdigão rarely exists below and just above the ridges [ $<600$  m above mean sea level (MSL)] despite uniform synoptic flow aloft ( $>1,000$  m) because of topographic steering. This three-dimensional (3D) nature of the flow is schematized in Fig. 2, drawn based on

measurements and simulations (see supplemental material). Notwithstanding this added complexity, basic flow phenomena characteristic of 2D valleys were still evident in Perdigão. Some flow processes studied by the Perdigão investigators are summarized in Fig. 3 on the backdrop of an idealized 2D double ridge with ridge-normal synoptic flow in the presence of a WT.

Two major mesoscale flow types are identified for complex terrain: thermal circulation due to heating and cooling of topography and synoptically forced flows through topographic features. The former includes upslope (anabatic) and downslope (katabatic) winds driven by buoyancy forces and upvalley and downvalley winds driven by temperature (and hence local pressure) gradients along the valley axis (Whiteman 1990). Flows emanated as a result of the interaction of topography with synoptic flow are also common, and such (mesoscale) flows need not follow the direction of thermal circulation (e.g., Fig. 2). Synoptic flows are energetic, and so are the ensuing circulations; thus, thermal circulation only appears under weak synoptic conditions. On the microscale, weak ( $\sim 1$  m  $s^{-1}$  at 2 m) thermally driven flows are possible via surface thermal inhomogeneities (Rife et al.

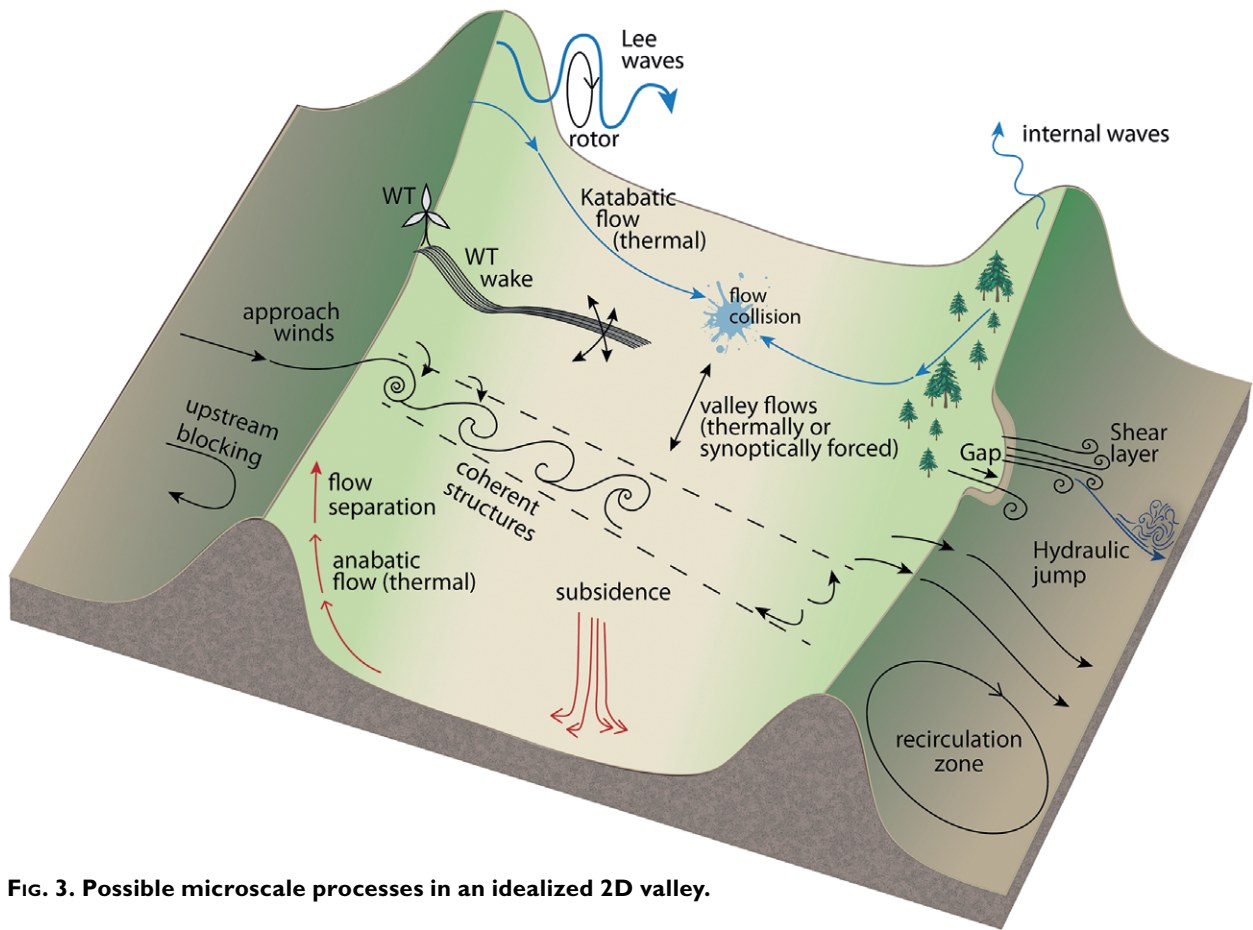


**FIG. 3. Possible microscale processes in an idealized 2D valley.**

2002), which are usually overshadowed by microscale flows ( $\geq 3 \text{ m s}^{-1}$ ) resulting from synoptic and mesoscale flows modified by the topography (Fig. 2).

When thermal circulation is dominant, nocturnal katabatic flows draining down from the mountains generate stable stratification in the valley. If exit flow is nonexistent or restricted, cold air so drained accumulates (or pools) in the valley. Internal wave breaking, collisions between different katabatic flows, seiching, and (directional) shear are common mixing mechanisms in cold pools (Fernando et al. 2015). In the morning, heating of the ground generates turbulent convection, and stable stratification is destroyed through a complex sequence of processes, leading to upslope flow and subsidence in the valley (Princevac and Fernando 2008). Separation of upslope flow may lead to deep convection and precipitation (Banta 1984). Evening transition begins with the radiative cooling of the ground, whence upslope flow transitions to downslope flow accompanied by a rich variety of flow phenomena (Hunt et al. 2003).

When the synoptic effects are dominant, flow behavior is governed by the stability of the flow, typically characterized by a gradient Richardson

number, a normalized mountain height, or height normalized by the Monin–Obukhov length scale (Kaimal and Finnigan 1994; Baines 1998). (In the Perdigão study, however, the flow and fluxes were strongly horizontally inhomogeneous, and thus the use of Monin–Obukhov framework could not be justified.) When the flow is neutrally stratified and the slopes are small, both the mean flow and turbulence are distorted in a thin layer over the hill (Jackson and Hunt 1975), but when the slope angles become larger flow separation and a recirculation zone are possible. When stably stratified, a myriad of flow phenomena [e.g., topographically trapped (lee) waves, progressive internal waves, rotors, hydraulic jumps, shear layers, recirculation and upstream blocking] may appear. It is customary to use the normalized mountain height to describe flows for this case (Baines 1998).

When a succession of 2D ridges is present, separated flows at the ridges and their interaction with the valley flow lead to a rich variety of unsteady phenomena (Rockwell 1983; Rapp and Manhart 2011). Possible flow types include coherent structures in shear layers, entrainment, recirculation, and interactions between separated flows (Cummins 2000). Topographic gaps

along the ridgeline are common, where additional flow phenomena appear. In neutral flows, shear layers at the gap interact with the lee slope and valley flows. Intriguing gap-flow phenomena are expected under stably stratified conditions (Gaberšek and Durran 2004), including leeside internal hydraulic jumps, flow jetting, gravity wave breaking, and undular bores (Baines 1987; Chen et al. 2004). In some cases, accelerating flow plunges down the slope as a compact current, while warming as it descends and causing vigorous mixing in cold pools (Mayr et al. 2007).

Of interest at the Perdigão campaign was the WT wake, especially the influence of atmospheric stability on wake dynamics. Stable stratification triggers unsteady and oscillatory phenomena that modulate wake signatures (Yi 2009; Barthelmie et al. 2016; Yang et al. 2017) whereas convective turbulence may obliterate wakes (e.g., Ching et al. 1995). The design of Perdigão incorporated measurements of entrainment, turbulence, trajectory, evolution, and recovery as well as acoustic propagation (Hubbard and Shepherd 1991) pertinent to WT wakes in complex terrain.

**SITE SELECTION AND CLIMATOLOGY.** In a workshop held in January 2011, the NEWA consortium announced that the primary land-based field campaign would be in complex terrain (see sidebar), with emphasis on flow up to the height of modern large WTs (~150 m). A 6–12-month extended monitoring program (EMP; with limited instrumentation operating continuously) followed by a 1–2-month intensive operational period (IOP; with all systems go) was recommended. The selected site was to represent challenges of wind resource and load estimations on a representative topography (e.g., steep slopes, flow separation). A moderate level of complexity was sought, to build upon Askervein and other microscale studies. In addition to traditional wind-energy-relevant parameters such as wind speed and turbulence profiles, the campaign was to measure spatiotemporal gradients and turbulent fluxes that affect the ABL stability and the surface pressure for testing of methods for coupling microscale and acoustic models. Evaluation of five candidate proposals led to the selection of the Perdigão site. Major deciding factors were the quasi-2D double-parallel-ridge topography, approximate ridge-normal annual wind climatology and horizontally isotropic turbulence (see supplemental material), the presence of only a few but disparate land-cover types, accessibility, local community support, a single WT (ENERCON; 2-MW/82-m diameter) operational on the southern ridge, and years of meteorological data available from a 100-m mast collocated with the WT.

## EVOLUTION OF A MEGAPROJECT

**P**erdigão is the largest of five NEWA campaigns funded by the European Research Area (ERA)-NET+, an EU funding instrument contributed by eight EU nations. The other NEWA campaigns are focused on forested hills (Kassel in Germany), offshore (northern Europe), large-scale topography (Alaiz Mountain, Spain), and heterogeneous forest (Hornamossen in Sweden). In NEWA, at least 10 years of mesoscale simulations with 2–3-km resolution will be downscaled to microscales (~100 m; seconds to hours) using statistical and dynamical (RANS and LES modeling) methods. Together with high-resolution field data, this will produce maps of wind statistics at microscale grid points and at wind turbine relevant heights, covering EU member states and their exclusive economic zones (Mann et al. 2017). NEWA will be a standard for site assessment and a key tool for manufacturers and developers, public authorities, and decision-makers.

The joining of U.S. groups in 2013 for the Perdigão project and ensuing funding from the U.S. NSF in 2015 under the large field campaign category of the NCAR EOL greatly enhanced the scope of the Perdigão project. Under the EOL/NSF umbrella, the following were funded: University of Notre Dame (UND), Cornell University (CU), University of California, Berkeley (UCB), University of Colorado Boulder (CU-Boulder), and University of Oklahoma (UO). The microscale research group of the U.S. Army Research Laboratory (ARL) joined in 2015 with significant resources. The main EU Perdigão participants were the DTU, University of Porto (UP), Institute of Science and Innovation in Mechanical and Industrial Engineering (INEGI), University of Oldenburg (UOL), Deutsches Zentrum für Luft-und Raumfahrt e.V. (DLR), and Portuguese Institute for Sea and Atmosphere (IPMA). A series of EU–U.S. group meetings and site visits between July 2013 and May 2015, a science workshop at University of Notre Dame during 25–26 September 2014, a pilot experiment in May–June 2015, and a comprehensive all-hands meeting in 10–13 May 2016 in Vila Velha de Ródão, a town abutting Vale do Cobrão, helped develop modus operandi for this large international field campaign. The supplementary material provides further details on participants. (Also see [www.eol.ucar.edu/field\\_projects/Perdigao](http://www.eol.ucar.edu/field_projects/Perdigao); for video, see <https://perdigao.fe.up.pt/>.)

The detailed climatology played the decisive factor in selecting the IOP period. The region has an average annual precipitation of ~760 mm, nearly 80% of which occurs between October and April owing to Atlantic extratropical depressions. May and June represent 12% of the total annual precipitation. High gusts (>25 m s<sup>-1</sup>) and hail events take place in winter and early spring, with occasional tornadic activity from November to January. During late autumn and winter, the minimum temperatures range from –4.7° to 16.8°C and the maximum from 2.7° to 25.4°C. The

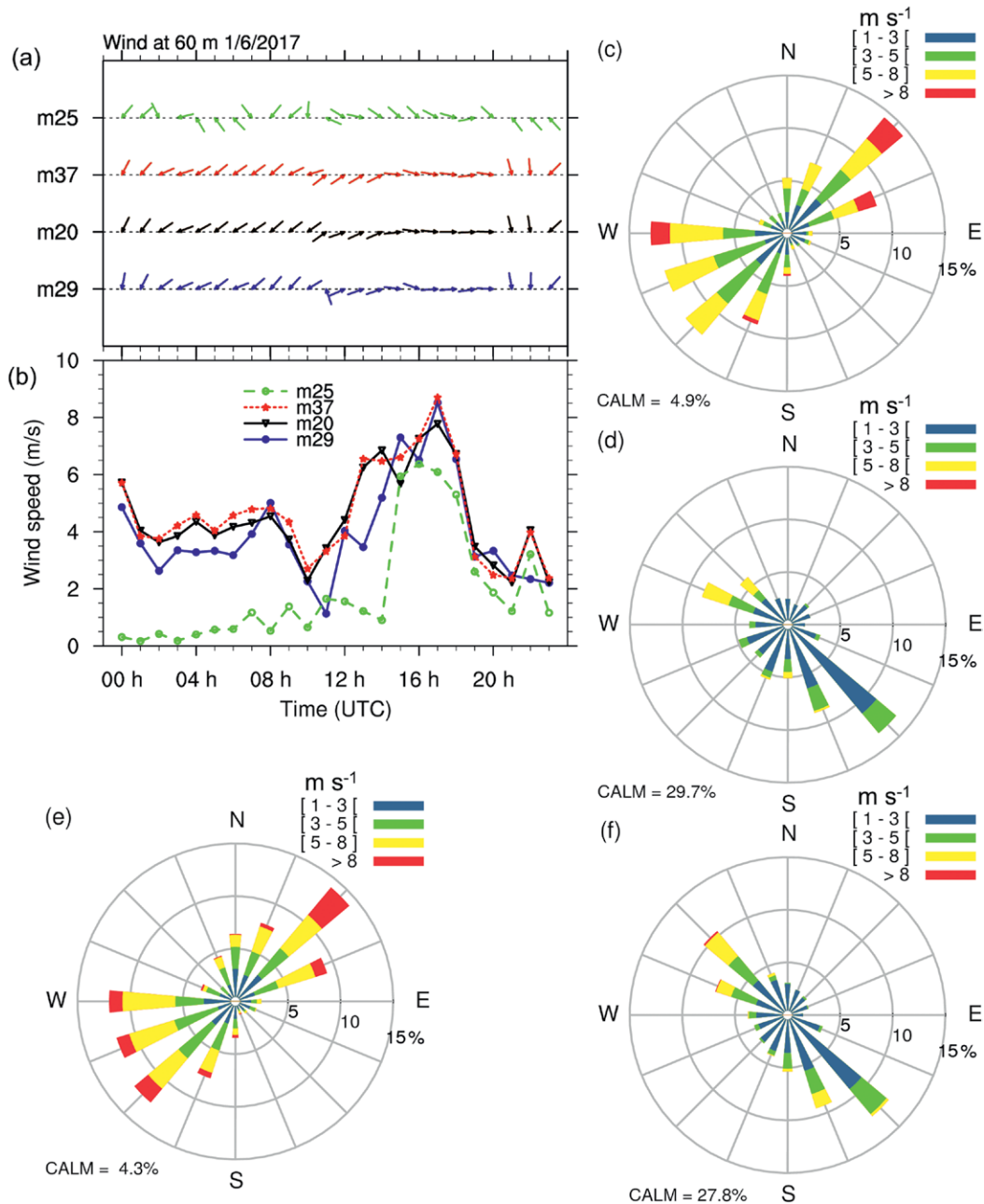


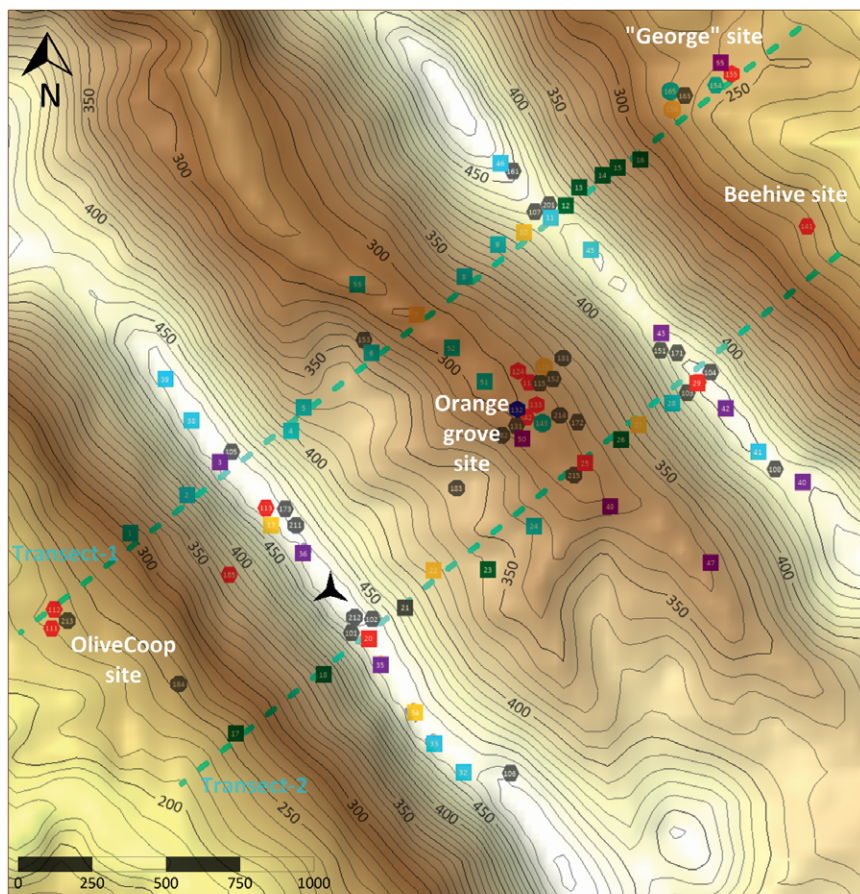
**FIG. 4.** Diurnal variation of 60-m (a) wind direction and (b) wind speed on 1 Jun, a clear-sky S3 day, at different towers on the ridge top (masts 37, 20, and 29) and in the valley (mast 25). Wind climatology of 60-m wind for S3 regime (21 days) days during the IOP, at (c) mast 20 and (d) mast 25. Wind climatology for the entire IOP period, at (e) mast 20 and (f) mast 25. Calm indicates the percentage of cases with wind speed  $< 1 \text{ m s}^{-1}$ . Mast locations are given in Fig. 5.

warmest and driest months prone to fire hazards are July and August, with maximum temperature on average exceeding  $30^{\circ}\text{C}$  for more than 21 days. Considering all, 1 May–15 June 2017 was selected for the IOP, with EMP covering the preceding 6 months. The summer break coincided with most IOP days, facilitating undergraduate and graduate student participation.

The daily climatology was crucial for operational planning, for which a weather type classification developed for the North Atlantic–western European sector ( $25^{\circ}$ – $70^{\circ}\text{N}$ ,  $30^{\circ}\text{W}$ – $10^{\circ}\text{E}$ ) by Santos et al. (2016) was used. Accordingly, there are eight synoptic types: S1, S2, and S3 (typical summertime types); W1, W2, and W3 (wintertime types); and B1 and B2 (blocking-like types). The daily synoptic classification

for the IOP is given in the supplemental material. The most frequent weather type during the IOP was S3 (44%), characterized by the Azores high and a high pressure belt over western Europe. On a typical clear-sky day of S3 regime, winds at 60 m exhibited a diurnal cycle of thermal forcing (Figs. 4a,b). At night and early morning, the winds are weak, with intensity increasing during early afternoon and peaking around 1700 UTC (1800 local time). The ridge-top wind is northeasterly (NE) until around 1000 UTC, shifting to southwesterly (SW) and then to westerly (W) around 1500 UTC before becoming northwesterly (NW) in the evening. The valley nocturnal winds are light and variable in direction, but as the upvalley flow developed during the day the flow direction stabilized to NW.

During the 21 days of the S3 regime, on the southern ridge line (mast 20, at 60 m, to be discussed next) the prevailing winds were W to SW ranging from 5 to 8 m s<sup>-1</sup>. Wind speeds greater than 8 m s<sup>-1</sup> are more frequent for W and NE winds (Fig. 4c). Overall, W to SW winds are dominant with a secondary maximum of NE on the ridges (Fig. 4c). In the valley, as expected, the wind speeds are lower, mostly ≤3 m s<sup>-1</sup>, and SE winds dominate (Fig. 4d). During the IOP period, the wind climatology indicates the dominance of ridge-normal component at the ridge top, similar to the S3 regime (Fig. 4e) but with higher wind intensities when compared to S3 days (Fig. 4c). In the valley the wind regime during the IOP (Fig. 4f) is also similar to S3 regime, as a consequence of the prevalence of the S3 regime during the IOP.



Remote sensing:  
 ● AERI ● Microwave radiometer ● Profiling Lidar ● Scanning Lidar ● Profiling Radar & RASS ● Profiling Radar  
 ● SODAR & RASS ● Water vapor DIAL ● Scintillometer ● Ceilometer

Meteorological masts:  
 ■ masts [2 m] ■ masts [10 m] ■ masts [20 m] ■ masts [30 m] ■ masts [60 m] ■ masts [100 m]

Sounding sites:  
 ● Radiosonde ● Tethersonde

Other  
 ● Noise Measurement terminal ● Seismometer ▲ Wind turbine

Source: <https://perdigao.fe.up.pt/>

**FIG. 5. Instrumentation deployed at the Perdigão campaign. Color-coded symbols indicate the type of instrumentation or tower type and the wind turbine (see legend below figure). Transects (1 and 2) and supersite locations (white lettering) are shown. A cluster of instrumentation was placed in supersites for focused process studies (also see Fernando et al. 2017).**

**INSTRUMENTS AND SITING.** The plurality of participating research groups permitted deployment of dense arrays of instruments (Fig. 5) to examine the microscale granularity of atmospheric structure over an area of ~4 km × 4 km, thus delineating flow phenomena depicted in Figs. 2 and 3. The instrument siting was strategized to help address science goals within logistical constraints; as such, instruments were mainly clustered in supersites, although some were spread around as needed. The observational

strategy relied on an intensive distributed network of 49 active meteorological towers (masts), 18 scanning and 8 profiling lidars, 1 water vapor differential absorption lidar (DIAL), 1 profiling radar, 1 profiling radar radio acoustic sounding system (RASS), 2 profiling sodar RASS, 2 radiosonde launch sites, 2 microwave radiometers (MWR), 2 tethered lifting systems (TLS), 1 scintillometer, 1 ceilometer, 9 acoustic sensors (microphones), 3 seismometers, 4 high-resolution microbarometers, and an aerosol particle-sizing instrument. Also deployed was the Collaborative Lower Atmospheric Profiling System (CLAMPS), which includes a scanning Doppler lidar, Atmospheric Emitted Radiance Interferometer (AERI), MWR, and a Vaisala WXT-530 weather transmitter (Wagner et al. 2019).

The meteorological towers carried a total of 195 three-component sonic anemometers, 55 temperature–humidity sensors, 22 barometers, 8 microbarometers, 14 radiometers, 17 CO<sub>2</sub>/H<sub>2</sub>O gas analyzers, 13 wetness sensors, 16 heat/moisture flux sensors, 5 thermohygrometers, and 3 pyrgeometers. The instruments were mounted at heights 2, 10, 20, 30, 40, 60, 80, and 100 m above ground level (AGL), depending on instrument availability and science needs. All towers recorded the local mean velocity, turbulence, heat, and momentum fluxes using sonic anemometers to help process and modeling studies. A subset of 16 of the towers directly measured all terms of the surface energy balance (flux towers). Given the complexity and heterogeneity of terrain, the measurement footprint of each tower was limited, and hence an array of towers was deployed along two representative cross sections. They included i) two cross-ridgeline transects, where the transect north of the orange site (approximate center of the campaign domain) was dubbed transect 1 and to the south was transect 2 (Fig. 5); ii) a line along each ridgeline; and iii) a line along the valley. Transect 1 passed through a ~700 m × 150 m × 55 m gap on the northern ridge. The campaign area was covered with a vegetative canopy of variable height (mean height ~10 m). Tower measurements included observations from both below and above the vegetative canopy. Even with this quantity of instrumentation, not all of the heights could be populated on each tower. The (standard) 10-m level always had a sonic anemometer (even when it was inside the canopy), and the 2-m level was used only on transects 1 and 2; the latter was decided based on in- and above-canopy flow interactions studies (e.g., Belcher et al. 2008) that called for measurements across the valley in the tree canopy and availability of sonics. Transects 1 and 2 offered studies of two

types of canopies with different leaf areas indices, with the latter affected by turbine wake when cross ridge flow was present. The along-ridge 2-m flow was deemphasized, as vegetation therein was sparse.

The National Center for Atmospheric Research (NCAR) in situ Data Acquisition Software (NIDAS) collected all tower data in real time through an extensive Wi-Fi network. Each sample was time tagged to microsecond resolution. Several towers on the ridge were augmented with seismometers and microbarometers to investigate high-resolution wind, pressure, ground vibrations, and seismic response (Hu et al. 2017). A set of lidars along with aerosol sizing instruments were codeployed in the Orange Grove site to compare wind speed profiles derived from Doppler lidars vis-à-vis direct-detection lidars under varying aerosol burdens.

Towers sampled the wind velocity, temperature, moisture, turbulence, and fluxes at 20 Hz. The TLS, radar wind profilers, MWR, sodar, and water vapor DIAL measured vertical profiles at selected positions and heights. A digital theodolite was used to survey the position and orientation of each instrument to a centimeter accuracy, allowing observations to be placed in the context of topographic maps and canopy structure measured from helicopter-based topographic laser scans prior to the experiment (Vasiljević et al. 2017).

Perdigão employed cutting-edge lidar technology. The coverage was unique and extensive, with multiple lidar units operating in coordinated or autonomous modes, measuring flow and turbulence at 25–75-m resolution. In this method, two or more scanning Doppler lidars (Wang et al. 2016; Vasiljević et al. 2016) are configured to synchronously retrieve the radial [line of sight (LoS)] component of winds at the probe volume. Controlled steering of beams by a master computer allows measurements within a hemispherical volume in a three-dimensional continuum of points from about 50 m out to a maximum of about 5 km. This coordination enables retrieval of two (two or more lidars) or all three (three or more lidars) wind velocity components without assuming horizontal homogeneity of the flow. Multilidar analysis produces full-scale, time-varying, 3D maps of wind velocities, turbulence, and Reynolds stresses, covering horizontal areas of tens of square kilometers and heights up to the ABL top (~1 km), following a myriad of measurement surfaces including “mobile” virtual towers (Calhoun et al. 2006). An antecedent pilot experiment was conducted at the same site in May–June 2015 to help configure lidar layout and fine-tune scanning patterns (Vasiljević et al. 2017).

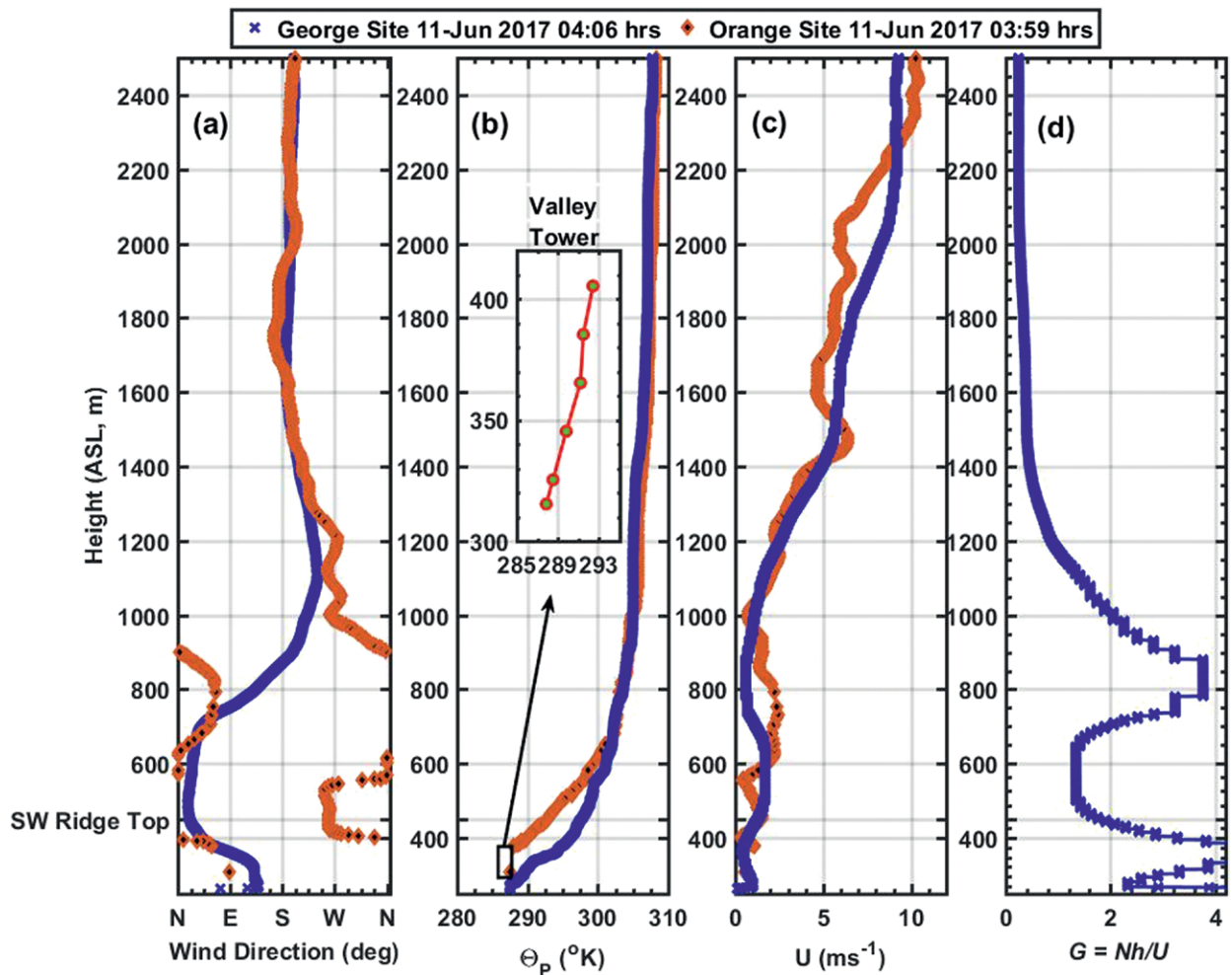


FIG. 6. Radiosonde data on 11 Jun (by UND and NCAR), with southwesterly synoptic forcing  $\sim 0400$  UTC (weather type W3). Blue is outside the valley (George site), and orange is inside the valley (Orange Grove site). Inset shows the valley temperature at the 100-m tower (25). The  $\Theta_p$  is potential temperature. Sites are given in Fig. 5.

The research team operated out of a control center located in Alvaiade within the Vila Velha de Ródão municipality. Data arriving at the control center could be viewed in real time or near-real time. Decisions on day-to-day operations were made during a daily planning meeting after inspection of latest data, upon receiving project updates from participants, and reviewing weather forecasts from IPMA.

#### DATA COLLECTION AND USER ACCESS.

A data management working group selected by the science team was responsible for developing a workable data policy that echoed community consensus. It addressed the issues of using a common format, metadata structure and content, and dataset documentation. Data collected by the bevy of diverse sensors were uploaded to the Earth Observing Laboratory (EOL; United States), University of Porto (UPORTO; Portugal), or Technical University of Denmark (DTU;

Denmark) repositories. Standard data formats [e.g., Network Common Data Form (netCDF)] were encouraged, including documentation of metadata. All mast data were streamed to the control center and uploaded to EOL repository after quality control. Other datasets were collected using procedures defined by data producers and later uploaded to the archives depending on the scope. The archives are periodically synchronized to achieve consistency. As the datasets produced are in great number and in many different formats, an e-science computational platform that uses data servers, distributed network and web technologies is in place (Gomes et al. 2014) to assist users to locate datasets of interest. The users may explore data in the following:

- UPORTO (<http://perdigao.fe.up.pt>),
- United States ([www.eol.ucar.edu/field\\_projects/Perdigão](http://www.eol.ucar.edu/field_projects/Perdigão)), and
- EU ([www.neweuropeanwindatlas.eu](http://www.neweuropeanwindatlas.eu)).

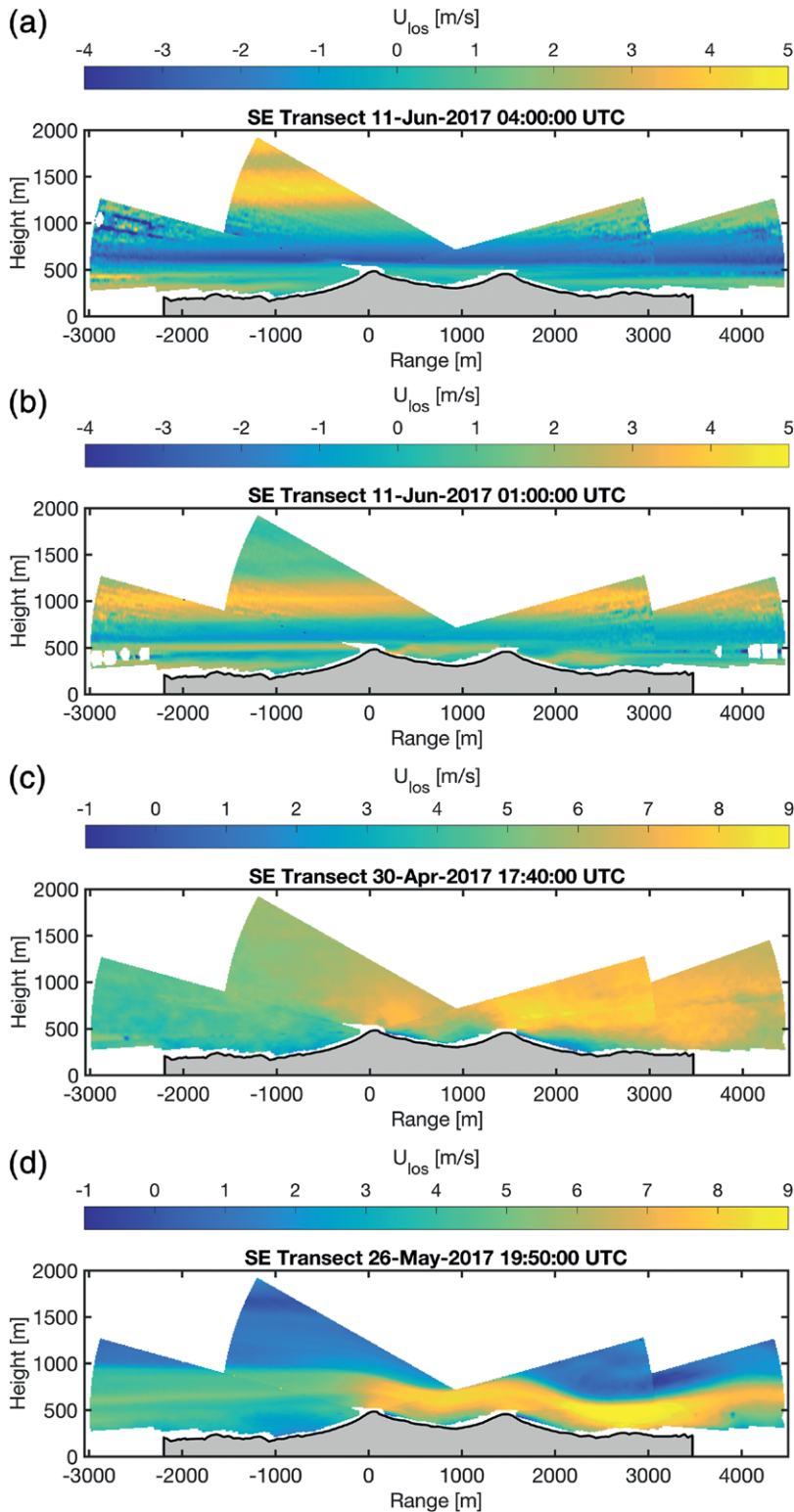


**FIG. 7.** Composite of quadruple scanning lidars, 10-min-averaged data by DTU (timestamp at the beginning of a period). All scanners measure in a vertical plane from SW on the left side to NE on the right side, perpendicular to the ridges, and the lidars are close to the summit of ridges (Fig. 5). The sign of the radial or LoS (along beam) velocities is positive (yellow) from left to right (southwesterly) in all cases and negative (dark blue) is opposite. (a),(b) Nocturnal stably stratified flow layers, (c) unstable flow during the late afternoon, and (d) wavy flow during early night. In (d),  $G = Nh/U \approx 0.1$  (based on 100-m tower 20 on the southern ridge) or  $G = 0.75$  (tower 29 on the northern ridge). The value of  $G$  for other cases is discussed in the text.

All parties agreed that Perdigão data should be publicly available after 15 June 2018, though it takes a longer time to completely mirror the databases.

### PRELIMINARY RESULTS.

**General flow patterns.** Mesoscale flows induced by the interaction of synoptic flow with regional terrain were prevalent, which, steered by local terrain, led to surprisingly complex microscale flows in Vale do Cobrão (Fig. 2; supplemental material). The W to SW synoptic flow produces N to NE mesoscale flow at the northern ridge, which, when assisted by valley thermal forcing, may produce stronger nocturnal valley flows than what is expected under pure thermal forcing. (Sometimes the synoptically and thermally driven valley flows are in opposite directions.) Figure 6 vividly depicts the SW synoptic flow at  $>1,000$  m MSL ( $\sim 6\text{--}10$  m  $s^{-1}$ ) and N to NE or W mesoscale circulation just above the ridges (400–700 m) based on radiosonde observations outside and within the valley, indicating a layered flow with shear. This is further corroborated by the range–height indicator (RHI) scans of quadruple lidar retrievals shown in Fig. 7a. Of the 20 scanning lidar units, four were optimized to work as a WindScanner system to generate vertical slices of flow as shown. Guided by the 2016 pilot experiment, four lidars were placed pairwise on top of the two ridges so both sides of the ridges could be scanned (Vasiljević et al. 2017).

In Fig. 6, the near-surface flow is down valley (E to SE), the same direction as the surface flow outside valley due to deflection of N mesoscale circulation by the northern hill, which generates a stratified flow parallel to the ridge (Fig. 2). The stable stratification within the valley is formed by radiative cooling, pooling of slope flows, and SE flow entering the valley. The valley stratification, however, is weaker ( $0.05 \text{ K m}^{-1}$ ; from tower 25) compared to outside ( $0.08 \text{ K m}^{-1}$ ; radiosondes) because of valley mixing processes depicted in Fig. 3 (Monti et al. 2002; Princevac et al. 2008).

The salient parameter describing stably stratified flow approaching normal to a 2D mountain of height  $h$  with an approach velocity  $U$  and buoyancy frequency  $N$  is the dimensionless mountain height  $G = Nh/U$  (Baines 1998). Evidently,  $G > 1$  is an indicator of the nonlinearity of flow. When  $G < 1$ , lee waves of wavelength much larger than  $h$  appear with an elongated separation bubble. When  $G \approx 1$ , resonant lee waves appear with a shorter wavelength. For  $G > 1$  the wavelengths become still shorter, rotors appear near the surface, and wave breaking occurs above the lee forming turbulent regions (Baines and Hoinka 1985; Silver et al. 2019). For  $0.5 < G < 2$  upstream propagating columnar wave modes appear. Upstream blocking occurs for  $G > 2$ , which is a 2D analog of the dividing streamline concept (Leo et al. 2016).

Several parameters are used to describe the relative importance of thermal and overlying flow (inertial) effects. Mason (1987) introduced  $F_M = (2U^2\theta/\Delta Bh^*)^{1/2}$  to describe the effacing of valley stable stratification by overlying flow. Here  $\Delta B$  is the buoyancy contrast between the valley and the overlying flow,  $h^*$  is a vertical scale of buoyancy perturbations, and  $\theta$  is the slope angle. Smaller Mason parameter  $F_M$  implies stronger stability at the ridge level and hence less penetration of flow into the valley or less ventilation (i.e., vertical exchange across the ridge level). A critical value demarcating synoptic and ventilation dominated regimes is not yet reported. Alternatively, some have argued that ridge-top ventilation is possible when  $G < G_c$  (Poulos et al. 2000), but a consistent critical value  $G_c$  has not emerged, with available data suggesting a range of 0.5–2.3.

Overall, the multiple-scanning Doppler–lidar approach provided an excellent space–time overview to place Perdigão flows in the context of above discussion. High space–time-resolution lidar observations of complex-terrain flow structures such as recirculation zones have been reported previously, but mostly using single-scanning lidars (Lange et al. 2017). In Fig. 7a, at 0400 UTC,  $G$  (~5) is very large at the ridge

level; thus trapped lee waves are not supported. In addition, the flow is conducive for upstream blocking, which is corroborated by upstream reverse flow. The buoyancy jump at the ridge level was sufficient to suppress ventilation. For Fig. 7a, small  $F_M$  (~0.1) aptly characterizes this weak ventilation. The layered flow downstream of the aft ridge is a classic case of strongly stably stratified flow. The vertical “disconnect” across the ridge top is clear from the change of wind direction at the ridge level from NE aloft to the SE in the valley. Figure 7b shows the scans taken three hours earlier (0100 UTC) with  $G \approx 1.1$  and  $F_M \approx 0.15$  at the ridge level, showing proximity to a (short wavelength) wave regime without ventilation. Recall that these meso- and microscale flows are sensitive to synoptic weather types (see supplemental material), and the conditions discussed above are a few of many possibilities.

Two examples of flow mapping using quadruple-lidar RHI scans along the transect 2 are shown in Figs. 7c and 7d. In both, the flow is generally from left to right (southwesterly), roughly normal to the ridges. In the late afternoon, a strong speedup of flow over the first ridge is seen (Fig. 7c), with a recirculation zone of light winds in the lee and an elevated shear layer over the valley. Higher wind speeds occur over the second ridge, again followed by an elongated recirculation region. The recirculating zone within the valley appears to be affected by the confinement, and the recirculation zone behind the first ridge does not reach the second. Two hours later, when stable stratification is developing rapidly, the flow becomes radically different (Fig. 7d). Here a large pool of almost stagnant air extends for more than a kilometer upstream of the first ridge, indicating possible upstream columnar wave modes and some blocking. A pool of stagnant air is also seen in the valley, pushed toward the second ridge and forming a dense air wedge. Recirculation zones in the wake of the ridges are shallower and shorter than during the daytime. The speedup on the second ridge is slightly larger than on the first, and, interestingly, the strongest winds occur a kilometer downstream of the second ridge. The velocities before the “blocked” region are generally weaker than after it, possibly due to larger flow area. The winds above 1,000 m MSL are generally very weak, or even slightly reversed. In this case the wavelength matches the inter-ridge spacing of 1,500 m, with a mean wind speed of  $7.5 \text{ m s}^{-1}$  in the wave zone of  $N \approx 0.03 \text{ s}^{-1}$ . The local  $N$  derived from the 100-m masts on ridge tops is less than a tenth of that above, but a few hours later into the night it does increase close to the wave oscillation frequency. The

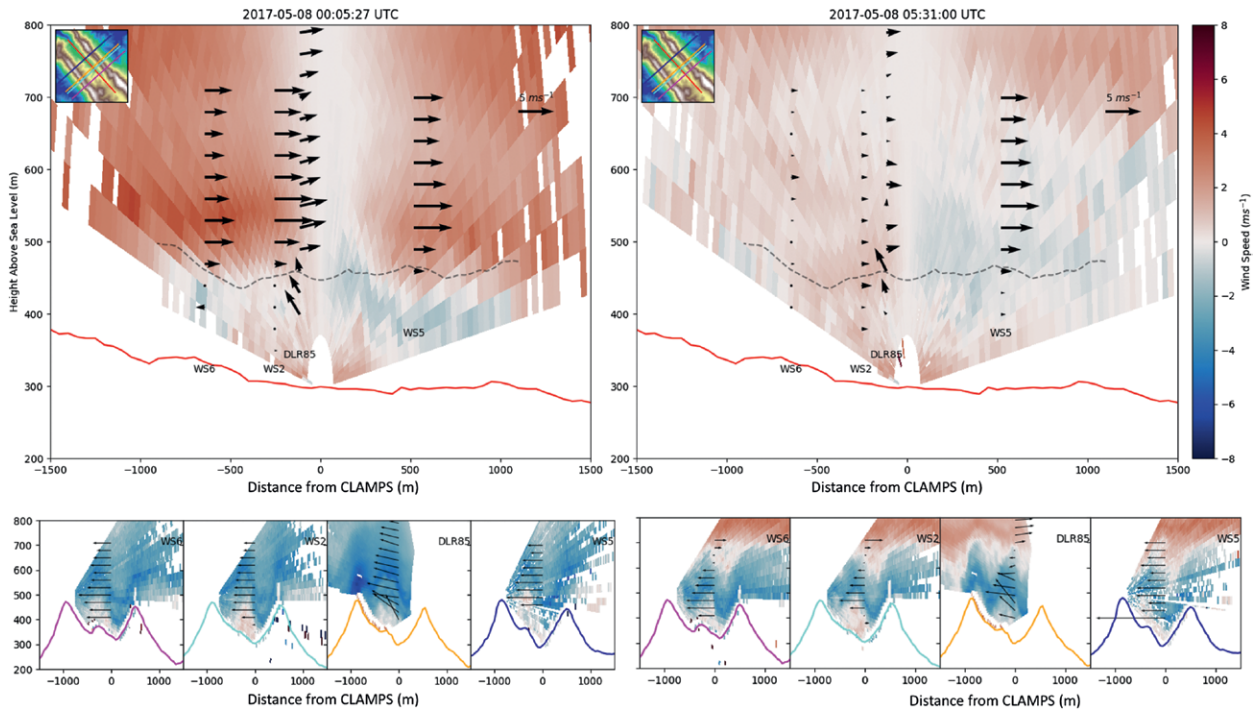


**FIG. 8.** (top) Data retrieved from the virtual towers at (left) ~0000 and (right) 0600 UTC 8 May using data from the OU (CLAMPS), DTU, and DLR lidars. The along-valley RHI from CLAMPS lidar (131 in Fig. 5, orange site) is projected such that it shows the along-valley component of the horizontal velocity with positive values indicating down-valley flow (flow toward positive  $x$  direction). The vectors show the component of the wind from the virtual tower retrievals projected into the along-valley plane. Note that DLR85 is the fully three-dimensional virtual tower from the DTU Windscanner system (WS2, WS5, and WS6 indicates lidars 102, 105, and 106, respectively, in Fig. 5; 102 and 106 are on the southern ridge and 105 is on the orange site). (bottom) The cross-valley components of the wind from four virtual towers and associated cross-valley RHI scans. The inserts in the top panels illustrate the terrain heights and the positions of the plotted cross sections.

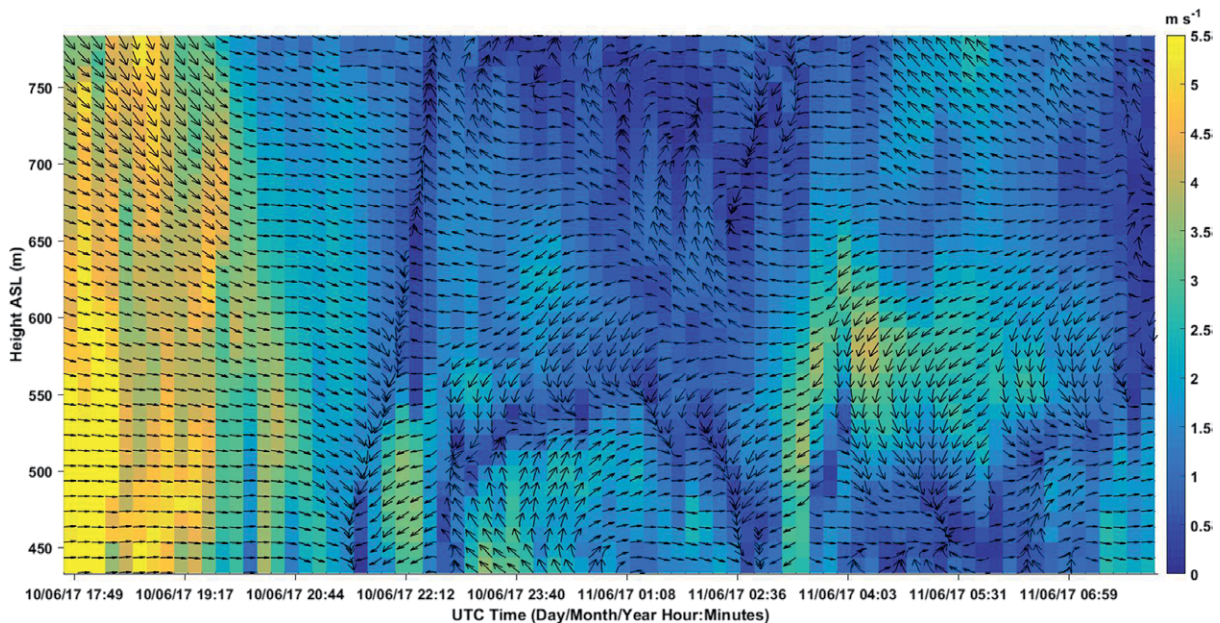


**FIG. 9.** Synchronized triple Doppler lidar measurements (by UND) at a virtual tower located in the middle of the gap of the northeast ridge along the NW transect. The color map shows the wind speed (see color bar) and arrows are the wind vectors. The times correspond to measurement times. The data were taken on 10–11 Jun with S3 weather type (measurement latitude and longitude:  $39.719^{\circ}\text{N}$ ,  $7.736^{\circ}\text{E}$ ).

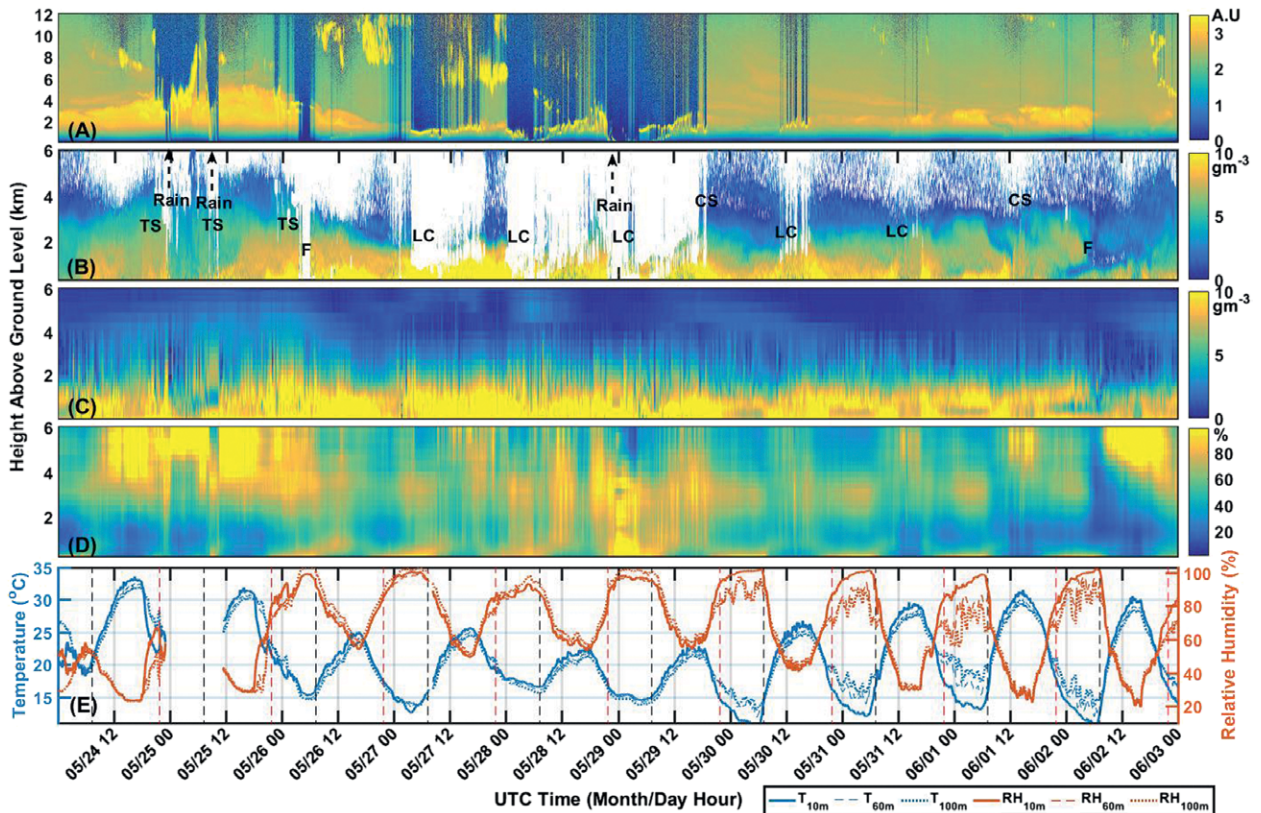


**FIG. 10.** (a) DIAL relative backscatter in aerosol units and (b) absolute humidity at the Orange Grove site (highlighting aerosol and cloud structures up to 12 km by NCAR); (c) AERI absolute humidity at the lower Orange Grove site (by UO); (d) MWR relative humidity (George site; outside the valley by UND); (e) relative humidity and temperature at different levels from the 100-m tower (mast 25) near DIAL and AERI. In (e), black dashed line indicates sunrise, and the orange line indicates sunset. Low clouds (LC); clear skies (CS); fog (F); thunderstorms (TS). Rain events are also indicated.

stability varies with height and evolves during the night. Three hours later (not shown), the wavelength decreased, a large bubble of slow moving air is developed in front of the second ridge, and the wavy jet left the ground after the ridge. Such striking lee waves appear during almost 50% of the IOP nights. A reverse flow on the northern ridgetop is (barely) evident in Fig. 7d.

Scans were also made to produce tall virtual towers with dual lidars (up to 600 m) on the ridges, along and across the valley, and to the northeast of the ridges. The results broadly elicited the dependence of valley flow on the weather type. An example of flow variability in the valley for 8 May is shown in Fig. 8. During that night, a temperature inversion forms inside the valley (Fig. ES5) that persisted until shortly after 0700 UTC, while sunrise was at 0515 UTC. In the early morning a strong downslope flow was observed while later on the winds veered, downslope flow weakened (Fig. 8), and the spatial variability within the valley increased. Wave patterns could be noted in the cross-valley flow throughout most

of the night. The virtual tower analysis allows the quantification of wind speeds in the waves, whereas RHIs give only the radial velocities along the beam.

A synchronized triple Doppler scanning lidar was deployed to obtain time series of true wind speed and wind direction at (steered) mobile virtual towers, focusing on gap flow on the northern ridge (see supplemental material). Figure 9 shows a time series cross section from a single virtual tower. In the evening, the flow in a layer of ~100-m thickness was W to NW, but it rotated to N, NE, S, and again to W flow from ~2100 UTC 10 June to 0100 UTC 11 June. Another spurt of changes initiated at ~0200 UTC. The flow above this layer also underwent rapid changes while reversing the flow at times. This complex velocity structure is consistent with data from proximate towers and radiosonde launches.

Atmospheric moisture content was measured using DIAL, MWR, and AERI inside the valley and MWR outside, supplemented by tower instruments. Figure 10 is a composite of DIAL backscatter (Fig. 10a) and absolute humidity (Fig. 10b), AERI

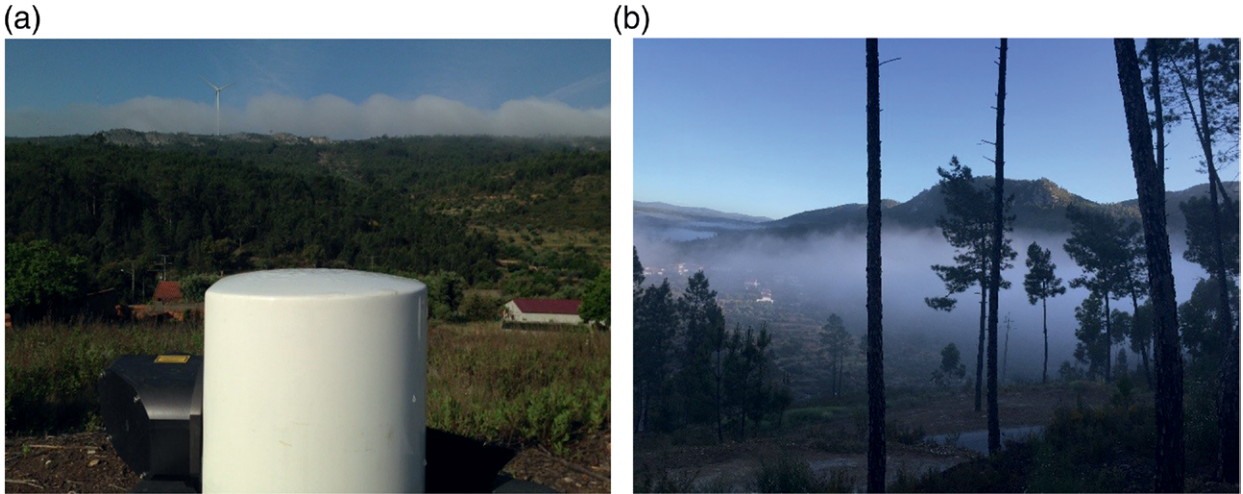


**FIG. 11. (a) Low-level clouds, penetrating below the WT, viewing from the northern ridge. (b) Thinner fog layer near the valley surface, viewing from Foz do Cobre (Fig. 5).**

absolute humidity (Fig. 10c), MWR water vapor outside the valley (Fig. 10d), and tower measurements (Fig. 10e) over 10 days dominated by the weather type S3. Thunderstorm conditions prevailed during the evenings of 24 and 25 May until about 1200 UTC 26 May, and a thick fog layer (~500–750 m) appeared both in the valley and north of it on the morning of 26 May with moisture extending up to several kilometers in height. Thunderstorms appear to be a moisture source for fog; interestingly, the surface temperature

gradient here is low, with relative humidity at saturation at all tower levels (Fig. 10e). Low clouds appeared on 27 May to about 29 May at the ridge height (Fig. 11a); this is masked as *white* in the DIAL humidity data because near-infrared light does not penetrate clouds or regions where absolute humidity exceeds  $10 \text{ g m}^{-3}$ . Elevated moisture layers occurred on 31 May and 1 June within and possibly outside the valley. In the morning of 2 June, after a day of clear skies, the moisture layer collapsed with little moisture aloft, and a layer of fog appeared near the ground both inside and outside the valley (Figs. 10a–d). Unlike on 26 May, the relative humidity here was 100% only at the lowest tower level with a stronger near-surface inversion, consistent with a thinner fog layer (Fig. 11b). Given the lack of other moisture sources, it is likely that radiative fog formed along the Ocreza River located in the northwest end of the valley was advected into the valley along the pathways in Fig. 2. The broad consistency between remote sensors and tower instruments here is noteworthy.

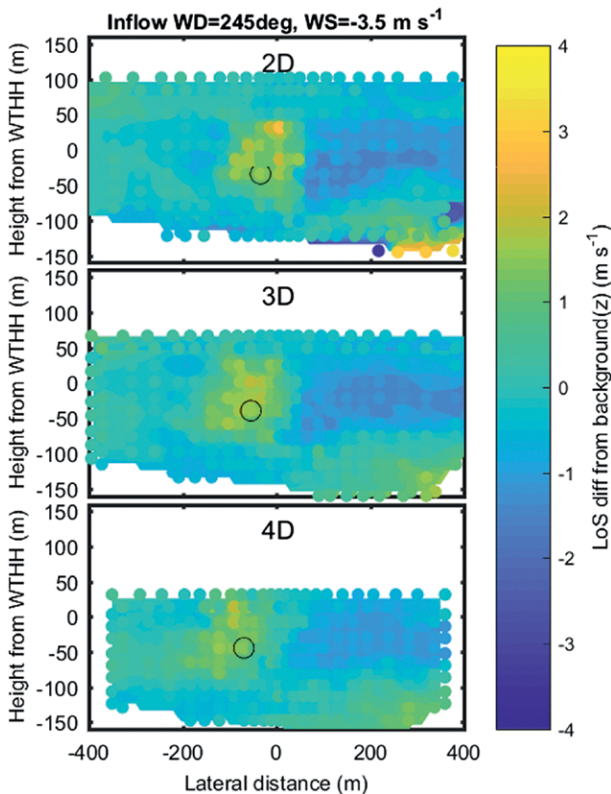


**FIG. 12. WT wake measured during 2335–2345 UTC 2 Mar 2017 (by CU lidars). Vertical slices of the LoS velocity expressed as velocity anomaly ( $\text{m s}^{-1}$ ) from the planar mean value at three downstream distances from the wind turbine (2D, 3D, 4D, where  $D$  is the WT rotor diameter). The LoS velocity is negative for winds approaching the lidar, thus positive values indicate weaker winds (and thus the WT wake). Each slice is perpendicular to the direction. The colored dots indicate the locations of lidar measured velocity deficit while the background velocity deficit fields are interpolated using cubic spline. The small black circle denotes the center of the WT wake, and the heights shown are distances from the wind turbine hub height (WTHH).**

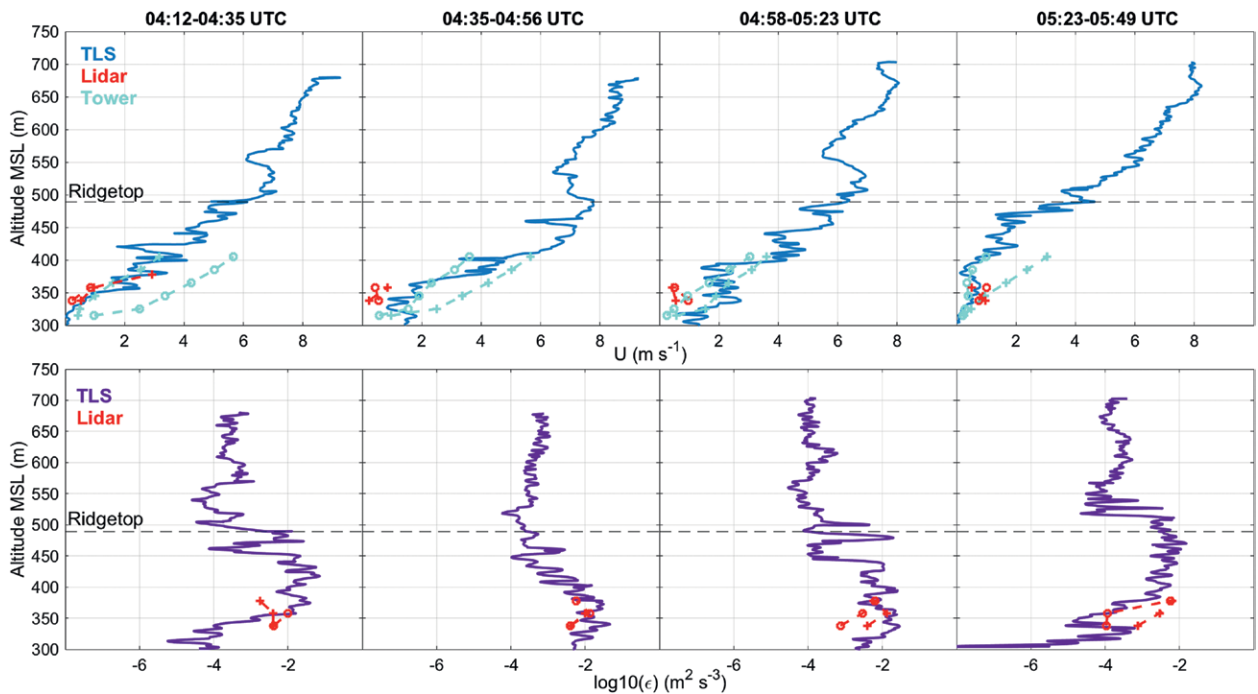


**FIG. 13.** Flights from the (CU-Boulder) TLS on the morning of 14 Jun. The TLS payloads included a 1-kHz hot-wire anemometer for measuring wind speed and a 1-kHz cold-wire for temperature fluctuations, in addition to 100-Hz measurements of wind speed, temperature, pressure, and humidity and 1-Hz GPS measurements of altitude, latitude, longitude, yaw, pitch, and roll. (top) Wind speed profiles are compared with those from the collocated tower (cyan) and lidar (red) at the beginning (circles) and end (plus signs) of the flights. (bottom) Values of  $\epsilon$  from TLS are compared with those from the Windcube v1 profiling lidar using the method of Bodini et al. (2018) at the beginning (circles) and end (plus signs) of the flight.

*Wind turbine wake measurements.* Perdigo science goals included measurements and (microscale and LES) modeling of WT wakes, for example, wake dimensions, asymmetry, velocity deficit, meander, turbulence, lofting and descent, and acoustic properties under varying stability conditions. To this end, Doppler lidar scans from the Orange Grove site covered multiple elevations and azimuth angles with telescoping increments with greatest resolution at or near the WT centerline. A full suite of scans, in addition to velocity–azimuth display (VAD) and RHI scans, were completed every 10 min. Out of 21,000 such scans in the entire campaign, 2,000 exhibited WT wake signatures (Barthelmie et al. 2018). During the IOP, many more scans were conducted using additional lidars. Observed signatures included wake lofting, advection at almost constant altitude above the sea level, and wake following the terrain (descending into the valley). Figure 12 shows an example of measured and interpolated velocity deficits in the WT wake. The along-beam (LoS) wind speed just upstream of the WT is  $\sim 3.5 \text{ m s}^{-1}$ , and conditions are stable. Vertical slices of LoS velocity deficit perpendicular to the wake direction are expressed as a function of the

number of rotor diameters  $D$  ( $=82 \text{ m}$ ) downstream. The wake remains aloft as it advects downwind such that at  $2D$  the wake velocity deficit is approximately  $2 \text{ m s}^{-1}$  and the wake is centered almost at the WT hub height. Farther downstream (i.e., at  $3D$  and  $4D$ ), the wake remains aloft but the center moves slightly downward while the shape becomes less circular and the velocity deficit gradually decreases.

Wake turbulence, for example, the turbulent kinetic energy dissipation  $\epsilon$ , was profiled by a hot or cold wire package attached to the TLS. Retrievals of  $\epsilon$  from the TLS [for the techniques, see Piper and Lundquist (2004) and Lundquist and Bariteau (2015)] located at the Lower Orange site about  $10D$  downwind of the WT are compared with  $\epsilon$  from a collocated lidar in Fig. 13. Elevated levels of  $\epsilon$  (locally) were observed at the proximity of WT heights, which can be related to either the advection of wake into the TLS measurement volume or increased production of turbulence at the ridgetop by shear. As seen in the successive flights on the morning of 14 June, wind speeds above the ridge top exceed those within the valley, while  $\epsilon$  is highest within the valley and below the ridge top. The altitudes of maximum  $\epsilon$  correspond to the altitudes

at which the WT wake was observed simultaneously by the scanning lidars, suggesting that enhanced dissipation in the WT wakes extends farther downwind of the WT than previously acknowledged (Lundquist and Bariteau 2015).

Acoustic propagation from WTs is strongly dependent on the local flow, stratification, and terrain. Theoretical and numerical modeling of meteorological effects on sound propagation have demonstrated how stratification and velocity profiles can profoundly influence acoustics (Zhu et al. 2005; Ovenden et al. 2009). These studies also advocated for reliable field data for model validation. In this regard, coplanar

continuous RHI scans of inflow and WT wake by two lidars in the plane of the wind direction over the entire IOP, supplemented by concurrent noise measurements at five fixed locations, provided valuable information. Further, a serendipitous shutdown of WT allowed delineation of wake evolution and acoustic response with and without the WT.

The WT shutdown occurred between 0400 and 0510 UTC 22 May. In the record shown in Fig. 14, at 0342 UTC, a SW low-level jet in the nocturnal boundary layer impinged on the WT with strong shear and inclination to the rotor plane. Thereafter, the jet followed the orography into the valley, and ascended

toward the second ridge. A pronounced wake was evident at 0350 UTC, which propagated into the valley with a wind speed deficit larger than 50% up to 5D or more downstream (cf. Figs. 12 and 13). When the WT was shut down 10 min later, the wake disappeared from the lidar scans, and when it started operating again after 0510 UTC the wake reappeared.

At different distances from the wind turbine, the WT sound was best noticeable in the 80-Hz one-third octave filter (Fig. 15). The signal attenuated with growing distance from the WT, and dropped remarkably by 15–20 dB at all locations during the shutdown time. The 80-Hz sound is discernible even at a distance of 942 m within the valley with a level of 30 dB.

**MODELING.** Improvement of microscale and turbine-wake models is a central task of NEWA; hence numerical modeling was a part of the planning, execution, and data analysis phases of the Perdigão campaign (Veiga Rodrigues et al. 2016; Vasiljević et al. 2017). In one study, the

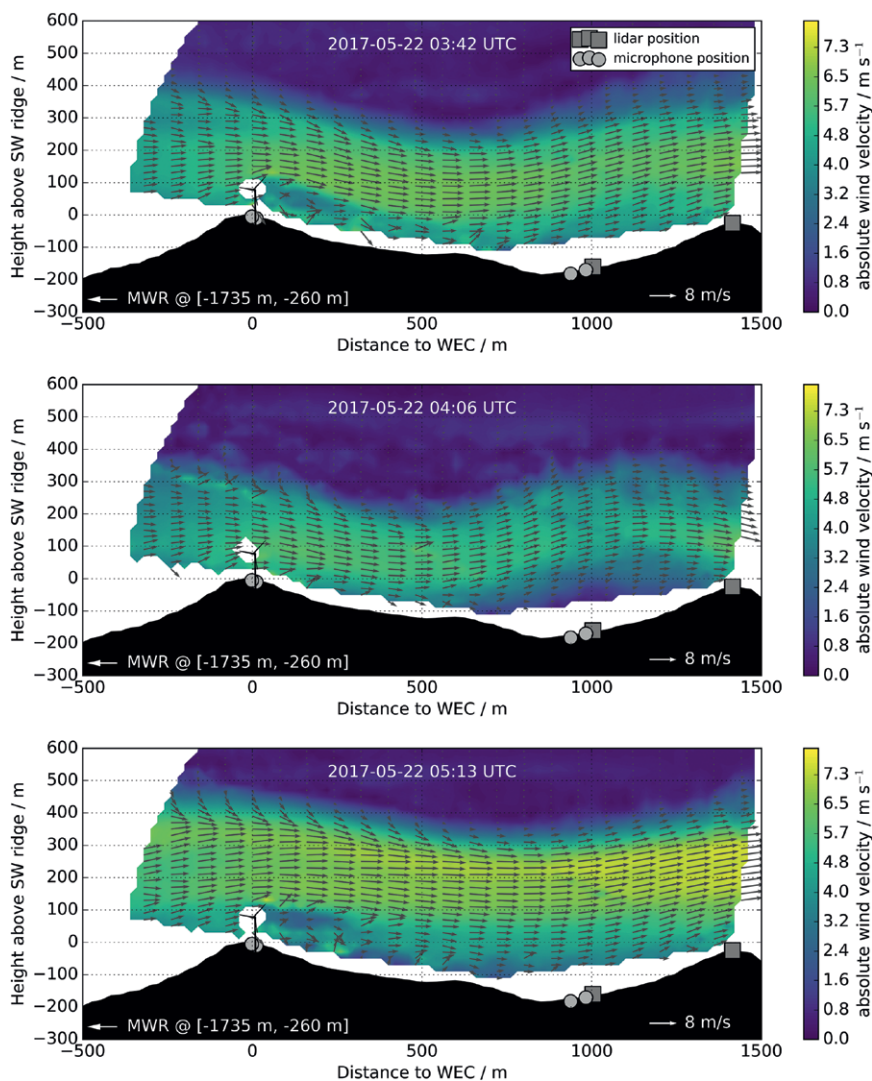


**FIG. 14.** Coplanar dual scans (10-min-averaged flow field) by DLR in a cross section of the Perdigão valley, in plane with the WT. (top) WT operating; (middle) WT shutdown; (bottom) WT operating again. The arrows indicate the flow direction in the plane and the color shading represents the absolute wind velocity. During this period,  $N = 1.7 \times 10^{-2} \text{ s}^{-1}$  measured by the upstream MWR (indicated).

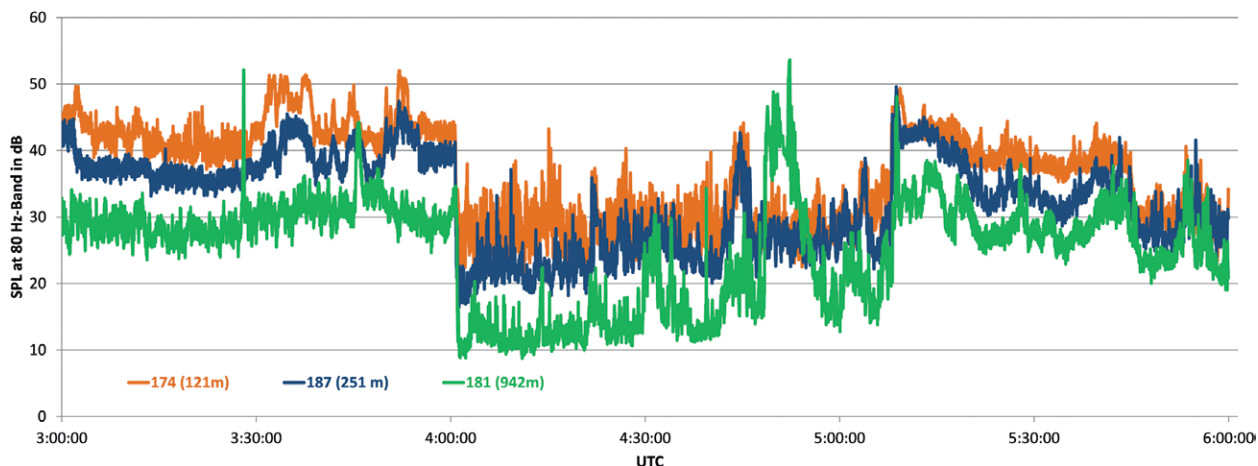


**FIG. 15. Acoustic intensity measurements by DLR based on one-third octave bandpass filter at 80 Hz. The measurements are taken at three different distances from the wind turbine (121 and 251 m on the ridge, and 942 m in the valley).**

output of simulations based on nested WRF, microscale, and turbine models (a model chain) was compared with Perdigão radiosonde observations. The Advanced Research version of the Weather Research and Forecasting Model (ARW-WRF, v3.8.1) was used to simulate mesoscale flow with three nested domains (37.5-, 7.5-, and 1.5-km grids). The 1.5-km domain output was further downscaled to microscales through one-way dynamical coupling using the WRF large-eddy simulation (LES; 300- and 150-m grids) and Ventos/M unsteady Reynolds-averaged Navier–Stokes (RANS) (40-m grid) models, as shown in Fig. 16a (see supplemental material for details). Figure 16b shows model–data comparisons for wind speed, direction, and temperature. Microscale simulations in general reproduced flow details better, but no model captured all the details of flow. Improvements to land surface dynamics and subgrid parameterizations of the microscale models are being pursued.

In a second study focusing on turbine wake, simulations from mesoscale (6.7-km horizontal resolution) to microscale (10-m horizontal resolution) are performed with five nest levels in WRF. The WT is represented using a generalized actuator disk model at 10-m resolution (Aitken et al. 2014; Mirocha et al. 2014). Special attention is given to the development of appropriate length scales on each domain using the lateral perturbation technique of Muñoz-Esparza et al. (2018) and considering “gray zone” issues (Zhou and Chow 2014; see supplemental material). Figures 16c and 16d show a WT wake simulation in WRF LES at 10-m horizontal resolution for SW stably stratified flow, which captures (wake) coherent structures as well as upstream flow blocking well.

The wake descends into the valley under these stable conditions, similar to that seen in Fig. 14.

**EPILOGUE.** The Perdigão campaign was conceived by the needs of the burgeoning wind energy sector to provide high-fidelity forecasts at microscale resolution for complex terrain winds. Existing forecasting models are predicated by the scarcity of high-resolution data, and hitherto only a handful of comprehensive datasets are available at microscale resolution (e.g., Askervein). The Perdigão offered a reasoned extension of Askervein—flow in a nominally 2D double ridge of moderate complexity. The campaign was a trailblazer in multiple fronts: it used cutting-edge hardware (e.g., multiple lidar technology), software (rapid data transmittal and viewing, thus supporting adaptive control of the campaign), and an unprecedentedly dense network of instrumentation at microscale. Perdigão is the largest land-based field project that has been supported by EOL/NCAR hitherto, and it represented a veritable U.S.–EU partnership. While innovative technologies were adopted, the Perdigão team admits that at present the old-fashioned mast-based wind sensors are as versatile and perhaps more robust with regard to durability, operability, accessible scales, and cost. Some of the EU towers were left operational to cover data over an annual cycle. Perdigão represented diversity of gender, countries, nationalities, institutions, scientists, staff, disciplines, and students. Notwithstanding the prima facie configuration of a parallel double ridge with ridge-normal flow, the flow in the valley and surroundings were strongly 3D because of the valley end effects, nearby mountains, and topographic/thermal inhomogeneities. This article described

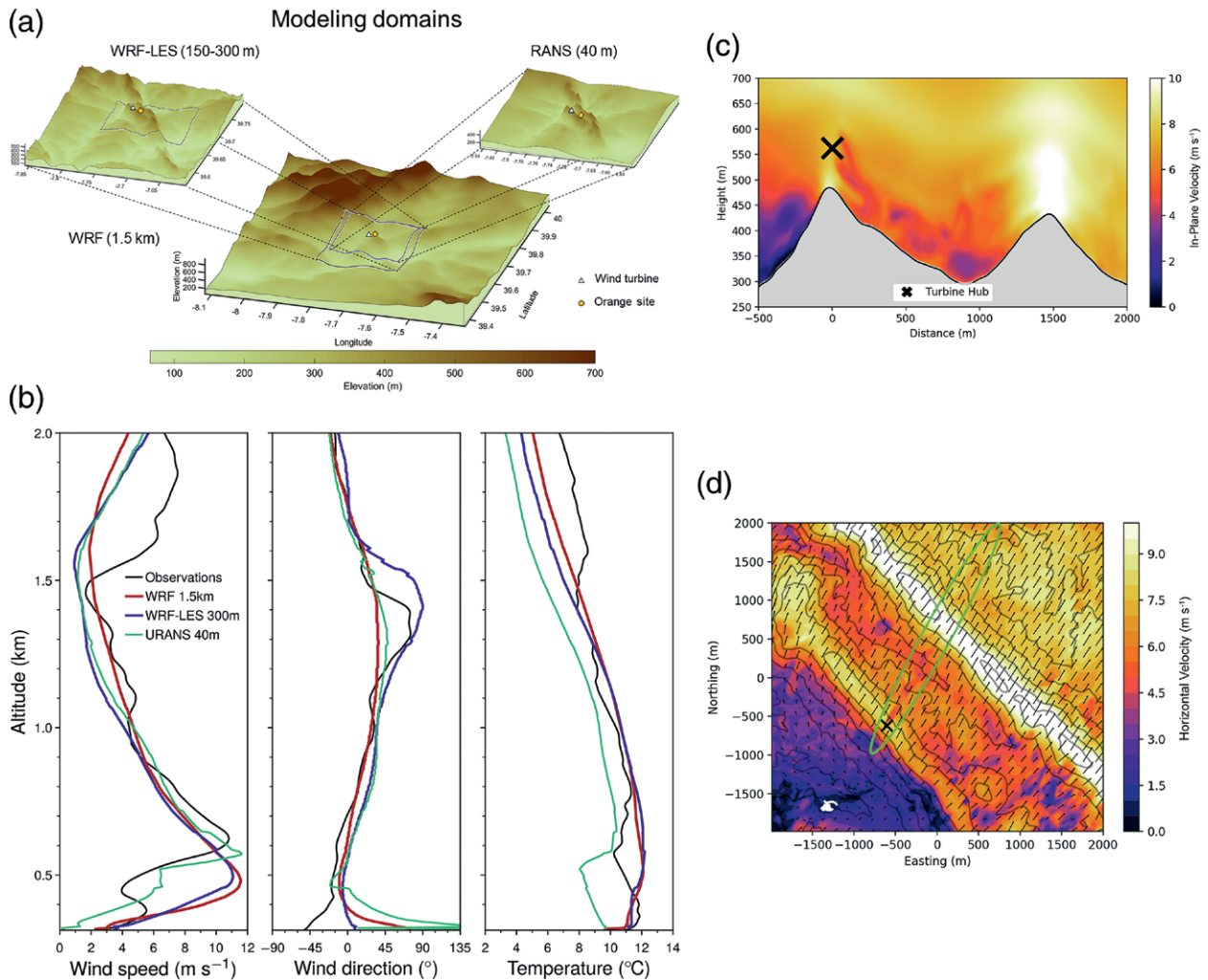


**FIG. 16.** (a) Downscaled topographic maps of domains used in the meso- to microscale model chain. The locations of two measurement sites used for comparisons in Fig. 16b are indicated (by UP and UND). (b) Comparison of the measured (left) wind speed, (center) direction, and (right) temperature in the lower atmosphere with WRF, WRF LES, and RANS- Ventos/M models at 2318 UTC 18 May 2017. The simulation started at 1200 18 May and covered 24 h (6-h spinup is considered within this period). (c) Vertical slice across the valley showing in-plane velocity contours ( $\text{m s}^{-1}$ ) and the turbine wake at 2136 UTC 21 May for nested WRF LES at 10-m horizontal resolution. Wind turbine location is indicated by  $\times$  (by UCB). (d) Plan view of the horizontal velocity ( $\text{m s}^{-1}$ ) of (c) at approximately 80 m above the ground level for nested WRF LES. Topographic contours (black) are shown at 50 m intervals. Turbine wake is outlined with green oval (by UCB)

campaign details and a preview of initial results, as a precursor to many forthcoming journal articles. The comprehensive (mirrored) databases, supporting documentation (including a project movie), and continuous updates to the permanent archives will help scores of current and future researches in fundamental studies and numerical simulations.

**ACKNOWLEDGMENTS.** The Perdigão was primarily funded by the U.S. National Science Foundation, European Commission's ERANET+, Danish Energy Agency, German Federal Ministry of Economy and Energy, Portugal

Foundation for Science and Technology, U.S. Army Research Laboratory, and the Israel Binational Science Foundation. Perdigão would not have been possible without the alliance of many personnel and entities, which are listed in the supplemental material. This part of the supplemental material provides details of the funding/grant numbers.

## REFERENCES

Aitken, M. L., B. Kosović, J. D. Mirocha, and J. K. Lundquist, 2014: Large eddy simulation of wind turbine wake dynamics in the stable boundary layer using

- the Weather Research and Forecasting Model. *J. Renewable Sustainable Energy*, **6**, 033137, <https://doi.org/10.1063/1.4885111>.
- Alfredsson, P. H., and A. Segalini, 2017: Wind farms in complex terrains: An introduction. *Philos. Trans. Roy. Soc. London*, **375A**, 20160096, <https://doi.org/10.1098/rsta.2016.0096>.
- Ayotte, K. W., 2008: Computational modelling for wind energy assessment. *J. Wind Eng. Ind. Aerodyn.*, **96**, 1571–1590, <https://doi.org/10.1016/j.jweia.2008.02.002>.
- Baines, P. G., 1987: Upstream blocking and airflow over mountains. *Annu. Rev. Fluid Mech.*, **19**, 75–95, <https://doi.org/10.1146/annurev.fl.19.010187.000451>.
- , 1998: *Topographic Effects in Stratified Flows*. Cambridge University Press, 482 pp.
- , and K. P. Hoinka, 1985: Stratified flow over two-dimensional topography in fluid of infinite depth: A laboratory simulation. *J. Atmos. Sci.*, **42**, 1614–1630, [https://doi.org/10.1175/1520-0469\(1985\)042<1614:SFOTDT>2.0.CO;2](https://doi.org/10.1175/1520-0469(1985)042<1614:SFOTDT>2.0.CO;2).
- Banta, R. M., 1984: Daytime boundary-layer evolution over mountainous terrain. Part 1: Observations of the dry circulations. *Mon. Wea. Rev.*, **112**, 340–356, [https://doi.org/10.1175/1520-0493\(1984\)112<0340:DBLEOM>2.0.CO;2](https://doi.org/10.1175/1520-0493(1984)112<0340:DBLEOM>2.0.CO;2).
- Barthelmie, R. J., P. Doubrawa, H. Wang, G. Giroux, and S. C. Pryor, 2016: Effects of an escarpment on flow parameters of relevance to wind turbines. *Wind Energy*, **19**, 2271–2286, <https://doi.org/10.1002/we.1980>.
- , S. C. Pryor, N. Wildmann, and R. Menke, 2018: Wind turbine wake characterization in complex terrain via integrated Doppler lidar data from the Perdigão experiment. *J. Phys.: Conf. Ser.*, **1037**, 052022, <https://doi.org/10.1088/1742-6596/1037/5/052022>.
- Belcher, S. E., and J. C. R. Hunt, 1998: Turbulent flow over hills and waves. *Annu. Rev. Fluid Mech.*, **30**, 507–538, <https://doi.org/10.1146/annurev.fluid.30.1.507>.
- , J. J. Finnigan, and I. N. Harman, 2008: Flows through forest canopies in complex terrain. *Ecol. Appl.*, **18**, 1436–1453, <https://doi.org/10.1890/06-1894.1>.
- Berg, J., J. Mann, A. Bechmann, M. S. Courtney, and H. E. Jørgensen, 2011: The Bolund experiment, part I: Flow over a steep, three-dimensional hill. *Bound.-Layer Meteor.*, **141**, 219–243, <https://doi.org/10.1007/s10546-011-9636-y>.
- Bodini, N., J. K. Lundquist, and R. K. Newsom, 2018: Estimation of turbulence dissipation rate and its variability from sonic anemometer and with Doppler lidar during the XPIA field campaign. *Atmos. Meas. Tech.*, **11**, 4291–4308, <https://doi.org/10.5194/amt-11-4291-2018>.
- Boyer, D. L., and P. A. Davies, 2000: Laboratory studies of orographic effects in rotating and stratified flows. *Annu. Rev. Fluid Mech.*, **32**, 165–202, <https://doi.org/10.1146/annurev.fluid.32.1.165>.
- Brighton, P. W. M., 1978: Strongly stratified flow past three-dimensional obstacles. *Quart. J. Roy. Meteor. Soc.*, **104**, 289–307, <https://doi.org/10.1002/qj.49710444005>.
- Calhoun, R., R. Heap, M. Princevac, R. Newsom, H. Fernando, and D. Ligon, 2006: Virtual towers using coherent Doppler lidar during the Joint Urban 2003 dispersion experiment. *J. Appl. Meteor. Climatol.*, **45**, 1116–1126, <https://doi.org/10.1175/JAM2391.1>.
- Castro, F. A., J. M. L. M. Palma, and A. S. Lopes, 2003: Simulation of the Askervein Flow. Part 1: Reynolds averaged Navier–Stokes equations ( $k$ - $\epsilon$  turbulence model). *Bound.-Layer Meteor.*, **107**, 501–530, <https://doi.org/10.1023/A:1022818327584>.
- Chen, Y., F. L. Ludwig, and R. L. Street, 2004: Stably stratified flows near a notched transverse ridge across the Salt Lake valley. *J. Appl. Meteor.*, **43**, 1308–1328, [https://doi.org/10.1175/1520-0450\(2004\)043<1308:SSFNAN>2.0.CO;2](https://doi.org/10.1175/1520-0450(2004)043<1308:SSFNAN>2.0.CO;2).
- Ching, C. Y., H. J. S. Fernando, and A. Robles, 1995: Breakdown of line plumes in turbulent environments. *J. Geophys. Res.*, **100**, 4707–4713, <https://doi.org/10.1029/94JC02701>.
- Clifton, A., M. H. Daniels, and M. Lehning, 2014: Effect of winds in a mountain pass on turbine performance. *Wind Energy*, **17**, 1543–1562, <https://doi.org/10.1002/we.1650>.
- Cummins, P. F., 2000: Stratified flow over topography: Time-dependent comparisons between model solutions and observations. *Dyn. Atmos. Oceans*, **33**, 43–72, [https://doi.org/10.1016/S0377-0265\(00\)00044-0](https://doi.org/10.1016/S0377-0265(00)00044-0).
- Doran, J. C., J. D. Fast, and J. Horel, 2002: The VTMX 2000 campaign. *Bull. Amer. Meteor. Soc.*, **83**, 537–551, [https://doi.org/10.1175/1520-0477\(2002\)083<0537:TVC>2.3.CO;2](https://doi.org/10.1175/1520-0477(2002)083<0537:TVC>2.3.CO;2).
- Fernando, H. J. S., 2010: Fluid dynamics of urban atmospheres in complex terrain. *Annu. Rev. Fluid Mech.*, **42**, 365–389, <https://doi.org/10.1146/annurev-fluid-121108-145459>.
- , and Coauthors, 2015: The MATERHORN: Unraveling the intricacies of mountain weather. *Bull. Amer. Meteor. Soc.*, **96**, 1945–1967, <https://doi.org/10.1175/BAMS-D-13-00131.1>.
- , J. K. Lundquist, and S. Oncley, 2017: Monitoring wind in Portugal’s mountains down to microscales. *Eos*, **98**, <https://doi.org/10.1029/2017EO074745>.
- Gaberšek, S., and D. R. Durran, 2004: Gap flows through idealized topography. Part I: Forcing by large-scale winds in the nonrotating limit. *J. Atmos. Sci.*, **61**, 2846–2862, <https://doi.org/10.1175/JAS-3340.1>.

- Gobiet, A., S. Kotlarski, M. Beniston, G. Heinrich, J. Rajczak, and M. Stoffel, 2014: 21st century climate change in the European Alps—A review. *Sci. Total Environ.*, **493**, 1138–1151, <https://doi.org/10.1016/j.scitotenv.2013.07.050>.
- Gomes, F., J. C. Lopes, J. L. Palma, and L. F. Ribeiro, 2014: WindS@ UP: The e-science platform for Wind-Scanner.eu. *J. Phys.: Conf. Ser.*, **524**, 012006, <https://doi.org/10.1088/1742-6596/524/1/012006>.
- Grubišić, V., and Coauthors, 2008: The terrain-induced rotor experiment: An overview of the field campaign and some highlights of special observations. *Bull. Amer. Meteor. Soc.*, **89**, 1513–1533, <https://doi.org/10.1175/2008BAMS24871>.
- Hu, W., S. Pryor, F. Letson, J. Tytell, and R. Barthelmie, 2017: Investigation of gust-seismic relationships and applications to gust detection. *J. Geophys. Res. Atmos.*, **122**, 140–151, <https://doi.org/10.1002/2016JD025858>.
- Hubbard, H. H., and K. P. Shepherd, 1991: Aeroacoustics of large wind turbines. *J. Acoust. Soc. Amer.*, **89**, 2495–2508, <https://doi.org/10.1121/1.401021>.
- Hunt, J. C. R., H. J. S. Fernando, and M. Princevac, 2003: Unsteady thermally driven flows on gentle slopes. *J. Atmos. Sci.*, **60**, 2169–2182, [https://doi.org/10.1175/1520-0469\(2003\)060<2169:UTDFOG>2.0.CO;2](https://doi.org/10.1175/1520-0469(2003)060<2169:UTDFOG>2.0.CO;2).
- Jackson, P. S., and J. C. R. Hunt, 1975: Turbulent wind flow over a low hill. *Quart. J. Roy. Meteor. Soc.*, **101**, 929–955, <https://doi.org/10.1002/qj.49710143015>.
- Kaimal, J. C., and J. J. Finnigan, 1994: *Atmospheric Boundary Layer Flows: Their Structure and Measurement*. Oxford University Press, 289 pp.
- Kiktev, D., and Coauthors, 2017: FROST-2014: The Sochi Winter Olympics International Project. *Bull. Amer. Meteor. Soc.*, **98**, 1908–1929, <https://doi.org/10.1175/BAMS-D-15-00307.1>.
- Kim, H. G., and V. C. Patel, 2000: Test of turbulence models for wind flow over terrain with separation and recirculation. *Bound.-Layer Meteor.*, **94**, 5–21, <https://doi.org/10.1023/A:1002450414410>.
- Lange, J., and Coauthors, 2017: For wind turbines in complex terrain, the devil is in the detail. *Environ. Res. Lett.*, **12**, 094020, <https://doi.org/10.1088/1748-9326/aa81db>.
- Leo, L. S., M. Y. Thompson, S. Di Sabatino, and H. J. S. Fernando, 2016: Stratified flow past a hill: Dividing streamline concept revisited. *Bound.-Layer Meteor.*, **159**, 611–634, <https://doi.org/10.1007/s10546-015-0101-1>.
- Li, J., L. Yang, X. Li, and H. Zheng, 2016: Visualization of local wind field based forest-fire's forecast modeling for transportation planning. *Multimedia Tools Appl.*, <https://doi.org/10.1007/s11042-016-3357-7>.
- Long, R. R., 1955: Some aspects of the flow of stratified fluids III: Continuous density gradients. *Tellus*, **7**, 341–357, <https://doi.org/10.3402/tellusa.v7i3.8900>.
- Lundquist, J. K., and L. Bariteau, 2015: Dissipation of turbulence in the wake of a wind turbine. *Bound.-Layer Meteor.*, **154**, 229–241, <https://doi.org/10.1007/s10546-014-9978-3>.
- Mann, J., and Coauthors, 2017: Complex terrain experiments in the New European Wind Atlas. *Philos. Trans. Roy. Soc.*, **375A**, 20160101, <https://doi.org/10.1098/rsta.2016.0101>.
- Mason, P. J., 1987: Diurnal variations in flow over a succession of ridges and valleys. *Quart. J. Roy. Meteor. Soc.*, **113**, 1117–1140, <https://doi.org/10.1002/qj.49711347804>.
- Mayr, G. J., and Coauthors, 2007: Gap flows: Results from the Mesoscale Alpine Programme. *Quart. J. Roy. Meteor. Soc.*, **133**, 881–896, <https://doi.org/10.1002/qj.66>.
- Mirocha, J., B. Kosovic, M. Aitken, and J. K. Lundquist, 2014: Implementation of a generalized actuator disk wind turbine model into WRF for large-eddy simulation applications. *J. Renewable Sustainable Energy*, **6**, 013104, <https://doi.org/10.1063/1.4861061>.
- Monti, P., H. J. S. Fernando, M. Princevac, W. C. Chan, T. A. Kowalewski, and E. R. Pardyjak, 2002: Observations of flow and turbulence in the nocturnal boundary layer over a slope. *J. Atmos. Sci.*, **59**, 2513–2534, [https://doi.org/10.1175/1520-0469\(2002\)059<2513:OO FATI>2.0.CO;2](https://doi.org/10.1175/1520-0469(2002)059<2513:OO FATI>2.0.CO;2).
- Muñoz-Esparza, D., R. D. Sharman, and J. K. Lundquist, 2018: Turbulent dissipation rate in the atmospheric boundary layer: Observations and WRF mesoscale modeling during the XPIA field campaign. *Mon. Wea. Rev.*, **146**, 351–371, <https://doi.org/10.1175/MWR-D-17-0186.1>.
- Ovenden, N. C., S. R. Shaffer, and H. J. S. Fernando, 2009: Impact of meteorological conditions on noise propagation from freeway corridors. *J. Acoust. Soc. Amer.*, **126**, 25–35, <https://doi.org/10.1121/1.3129125>.
- Palma, J. M. L. M., F. A. Castro, L. F. Ribeiro, A. H. Rodrigues, and A. P. Pinto, 2008: Linear and non-linear models in wind resource assessment and wind turbine micro-siting in complex terrain. *J. Wind Eng. Ind. Aerodyn.*, **96**, 2308–2326, <https://doi.org/10.1016/j.jweia.2008.03.012>.
- Piper, M., and J. K. Lundquist, 2004: Surface layer turbulence measurements during a frontal passage. *J. Atmos. Sci.*, **61**, 1768–1780, [https://doi.org/10.1175/1520-0469\(2004\)061<1768:SLTMDA>2.0.CO;2](https://doi.org/10.1175/1520-0469(2004)061<1768:SLTMDA>2.0.CO;2).
- Poulos, G. S., J. E. Bossert, T. B. McKee, and R. A. Pielke, 2000: The interaction of katabatic flow and mountain waves. Part I: Observations and idealized

- simulations. *J. Atmos. Sci.*, **57**, 1919–1936, [https://doi.org/10.1175/1520-0469\(2000\)057<1919:TIOKFA>2.0.CO;2](https://doi.org/10.1175/1520-0469(2000)057<1919:TIOKFA>2.0.CO;2).
- Princevac, M., and H. J. S. Fernando, 2008: Morning breakup of cold pools in complex terrain. *J. Fluid Mech.*, **616**, 99–109, <https://doi.org/10.1017/S0022112008004199>.
- , J. C. R. Hunt, and H. J. S. Fernando, 2008: Quasi-steady katabatic winds over long slopes in wide valleys. *J. Atmos. Sci.*, **65**, 627–643, <https://doi.org/10.1175/2007JAS2110.1>.
- Queney, P., 1948: The problem of airflow over mountains: A summary of theoretical studies. *Bull. Amer. Meteor. Soc.*, **29**, 16–26, <https://doi.org/10.1175/1520-0477-29.1.16>.
- Rapp, C., and M. Manhart, 2011: Flow over periodic hills: An experimental study. *Exp. Fluids*, **51**, 247–269, <https://doi.org/10.1007/s00348-011-1045-y>.
- Rife, D. L., T. T. Warner, F. Chen, and E. G. Astling, 2002: Mechanisms for diurnal boundary layer circulations in the great basin desert. *Mon. Wea. Rev.*, **130**, 921–938, [https://doi.org/10.1175/1520-0493\(2002\)130<0921:MFDBLC>2.0.CO;2](https://doi.org/10.1175/1520-0493(2002)130<0921:MFDBLC>2.0.CO;2).
- Rockwell, D., 1983: Oscillations of impinging shear layers. *AIAA J.*, **21**, 645–664, <https://doi.org/10.2514/3.8130>.
- Santos, J. A., M. Belo-Pereira, H. Fraga, and J. G. Pinto, 2016: Understanding climate change projections for precipitation over western Europe with a weather typing approach. *J. Geophys. Res. Atmos.*, **121**, 1170–1189, <https://doi.org/10.1002/2015JD024399>.
- Silver, Z., R. Dimitrova, T. Zsedrovits, P. G. Baines, and H. J. S. Fernando, 2019: Simulation of stably stratified flow in complex terrain: Flow structures and dividing streamline. *Environ. Fluid Mech.*, <https://doi.org/10.1007/s10652-018-9648-y>, in press.
- Strobach, K., 1991: *Unser Planet Erde-Usprung und Dynamik*. Gebruder Bornträger, 253 pp.
- Taylor, P. A., and H. W. Teunissen, 1983: ASKERVEIN '82: Report on the September/October 1982 Experiment to Study Boundary-Layer Flow Over Askervein, South Uist. Atmosphere Environment Service Research Rep. MSRB-83-8, 172 pp.
- , P. E. Mason, and E. Bradley, 1987: Boundary-layer flow over low hills. *Bound.-Layer Meteor.*, **39**, 107–132, <https://doi.org/10.1007/BF00121870>.
- Vasiljević, N., G. Lea, M. Courtney, J. P. Cariou, J. Mann, and T. Mikkelsen, 2016: Long-range Wind-Scanner system. *Remote Sens.*, **2016**, 896, <https://doi.org/10.3390/rs8110896>.
- , and Coauthors, 2017: Perdigoão 2015: Methodology for atmospheric multi-Doppler lidar experiments. *Atmos. Meas. Tech.*, **10**, 3463–2383, <https://doi.org/10.5194/amt-10-3463-2017>.
- Veiga Rodrigues, C., J. M. L. M. Palma, N. Vasiljevic, M. Courtney, and J. Mann, 2016: Coupled simulations and comparison with multi-lidar measurements of the wind flow over a double-ridge. *J. Phys.: Conf. Ser.*, **753**, 032025, <https://doi.org/10.1088/1742-6596/753/3/032025>.
- Wagner, T. J., P. M. Klein, and D. D. Turner, 2019: A new generation of ground-based mobile platforms for active and passive profiling of the boundary layer. *Bull. Amer. Meteor. Soc.*, <https://doi.org/10.1175/BAMS-D-17-0165.1>, in press.
- Walmsley, J. L., and P. A. Taylor, 1996: Boundary-layer flow over topography: Impacts of the Askervein study. *Bound.-Layer Meteor.*, **78**, 291–320, <https://doi.org/10.1007/BF00120939>.
- Wang, Y., C. M. Hocut, S. W. Hoch, E. Creegan, H. J. S. Fernando, C. D. Whiteman, M. Felton, and G. Huynh, 2016: Triple Doppler wind lidar observations during the mountain terrain atmospheric modeling and observations field campaign. *J. Appl. Remote Sens.*, **10**, 026015, <https://doi.org/10.1117/1.JRS.10.026015>.
- Whiteman, C. D., 1990: Observations of thermally developed wind systems in mountainous terrain. *Atmospheric Processes over Complex Terrain, Meteor. Monogr.*, No. 23, Amer. Meteor. Soc., 5–42.
- Wilczak, J., and Coauthors, 2019: The Second Wind Forecast Improvement Project (WFIP2): Observational field campaign. *Bull. Amer. Meteor. Soc.*, <https://doi.org/10.1175/BAMS-D-18-0035.1>, in press.
- Yang, B., and Coauthors, 2017: Sensitivity of turbine-height wind speeds to parameters in planetary boundary-layer and surface-layer schemes in the Weather Research and Forecasting Model. *Bound.-Layer Meteor.*, **162**, 117–142, <https://doi.org/10.1007/s10546-016-0185-2>.
- Yi, C., 2009: Instability analysis of terrain-induced canopy flows. *J. Atmos. Sci.*, **66**, 2134–2142, <https://doi.org/10.1175/2009JAS3005.1>.
- Zhou, B., and F. K. Chow, 2014: Nested large-eddy simulations of the intermittently turbulent stable atmospheric boundary layer over real terrain. *J. Atmos. Sci.*, **71**, 1021–1039, <https://doi.org/10.1175/JAS-D-13-0168.1>.
- Zhu, W. J., N. Heilskov, W. Z. Shen, and J. N. Sørensen, 2005: Modeling of aerodynamically generated noise from wind turbines. *J. Sol. Energy Eng.*, **127**, 517–528, <https://doi.org/10.1115/1.2035700>.

# Radar and Atmospheric Science: A Collection of Essays in Honor of David Atlas

Edited by Roger M. Wakimoto and Ramesh Srivastava



This monograph pays tribute to one of the leading scientists in meteorology, Dr. David Atlas. In addition to profiling the life and work of the acknowledged “Father of Radar Meteorology,” this collection highlights many of the unique contributions he made to the understanding of the forcing and organization of convective systems, observation and modeling of atmospheric turbulence and waves, and cloud microphysical properties, among many other topics. It is hoped that this text will inspire the next generation of radar meteorologists, provide an excellent resource for scientists and educators, and serve as a historical record of the gathering of scholarly contributions honoring one of the most important meteorologists of our time.

## Radar and Atmospheric Science: A Collection of Essays in Honor of David Atlas

Aug 2003. Meteorological Monograph Series, Vol. 30, No. 52;  
270 pp, hardbound; ISBN 1-878220-57-8; AMS code MM52.

**Price** \$100.00 list/\$80.00 member

**To place an order** point your Web browser to  
[www.ametsoc.org/amsbookstore](http://www.ametsoc.org/amsbookstore)

## AMS BOOKS

RESEARCH ◆ APPLICATIONS ◆ HISTORY

